# DESIGN, SIMULATION, AND FABRICATION OF LOW-COST INKJET ANTENNAS

A THESIS SUBMITTED TO
THE GRADUATE SCHOOL OF NATURAL AND APPLIED SCIENCES
OF
MIDDLE EAST TECHNICAL UNIVERSITY

BY

FEZA MUTLU

IN PARTIAL FULFILLMENT OF THE REQUIREMENTS
FOR
THE DEGREE OF MASTER OF SCIENCE
IN
ELECTRICAL AND ELECTRONICS ENG.

AUGUST 2016

Approval of the thesis:

**DESIGN, SIMULATION, AND FABRICATION OF LOW-COST INKJET ANTENNAS**

submitted by **FEZA MUTLU** in partial fulfillment of the requirements for the degree of **Master of Science in Electrical and Electronics Eng. Department, Middle East Technical University** by,

Prof. Dr. Gülbin Dural Ünver
Dean, Graduate School of **Natural and Applied Sciences** _____

Prof. Dr. Tolga Çiloğlu
Head of Department, **Electrical and Electronics Eng.** _____

Assoc. Prof. Dr. Özgür Ergül
Supervisor, **Elec. and Electronics Eng. Dept., METU** _____

**Examining Committee Members:**

Prof. Dr. Gülbin Dural Ünver
Electrical and Electronics Engineering Dept., METU _____

Assoc. Prof. Dr. Özgür Ergül
Electrical and Electronics Engineering Dept., METU _____

Prof. Dr. Gönül Turhan Sayan
Electrical and Electronics Engineering Dept., METU _____

Prof. Dr. Mustafa Kuzuoğlu
Electrical and Electronics Engineering Dept., METU _____

Assoc. Prof. Dr. Vakur Behçet Ertürk
Elec. and Electronics Engineering Dept., Bilkent University _____

**Date: 25.08.2016**

**I hereby declare that all information in this document has been obtained and presented in accordance with academic rules and ethical conduct. I also declare that, as required by these rules and conduct, I have fully cited and referenced all material and results that are not original to this work.**

Name, Last Name: FEZA MUTLU

Signature :

# ABSTRACT

## DESIGN, SIMULATION, AND FABRICATION OF LOW-COST INKJET ANTENNAS

Mutlu, Feza
M.S., Department of Electrical and Electronics Eng.
Supervisor : Assoc. Prof. Dr. Özgür Ergül

August 2016, 73 pages

In this study, low-cost inkjet-printed antennas are investigated from the design level to the end-product level. As a substrate, commercial photograph paper is used. Antennas working in various frequency bands are designed using a sophisticated simulation environment based on the multilevel fast multipole algorithm (MLFMA). Antennas are printed via standard, low-cost, and commercial printers using conductive 25% alloyed silver ink. After printing, a temperature curing process is applied in order to increase the conductivity of silver ink paths.

Four different types of antennas are proposed and studied. As the first type, an S-monopole antenna is designed for both 50 Ω input impedance and microchip input impedance. Measurement results show that 50 Ω tuned antenna resonates at 1.66 GHz with a reflection coefficient of -12.4 dB. As the second type, a small (5 cm x 5.3 cm) symmetric dipole antenna with the input impedance of 50 Ω is introduced. It resonates at 870 MHz with a reflection coefficient of -14 dB. As the third type, loop-meander antennas are proposed for radio

frequency identification (RFID) applications at ultra-high frequency (UHF; 865-868 MHz) band. First, a loop antenna which is conjugately matched to microchip impedance at 865 MHz is designed. The microchip is connected to the terminals of the antenna using conductive epoxy. Therefore, a working fabricated tag is obtained. Then, meander structures are added to the loop antenna as parasitic elements to increase the reading range of the antenna. For the read range tests, a simple measurement setup is developed. Reading range is measured for the loop-meander antennas using a reader which works in 865-868 MHz band with output power of 1W or 30 dBm (ATID AT870 Hand-Held UHF RFID reader). According to the measurement results, the maximum reading range is achieved as 60 cm. As the last and fourth type, cage-dipole antennas are designed by using genetic algorithms. An antenna that is matched to 50 $\Omega$ is measured, and it is observed that, it resonates at 1.56 GHz with a reflection coefficient of -23 dB. This antenna is re-designed for RFID applications to resonate at 865 MHz. Reading range tests are conducted on the developed setup and also on the human body. It is observed that the tag is satisfactorily identified at distances larger than 1.5 meters in a wide range of observation angles.

In addition to the designed and tested antennas, this thesis discusses low-cost inkjet printing steps, effects of curing time and temperature in inkjet printing, and importance of the impedance matching for RFID antennas.

Keywords: Inkjet Printing, Inkjet Antennas, Paper Substrate, Radio Frequency Identification, Low-Cost Antenna Design, Conductive Silver Ink, Reading Range Tests

# ÖZ

## DÜŞÜK-MALİYETLİ İNKJET ANTENLERİN TASARIM, BENZETİM VE ÜRETİMLERİ

Mutlu, Feza
Yüksek Lisans, Elektrik ve Elektronik Mühendisliği Bölümü
Tez Yöneticisi : Doç. Dr. Özgür Ergül

Ağustos 2016, 73 sayfa

Bu çalışmada, düşük maliyetli inkjet baskılı antenler tasarım aşamasından üretim aşamasına kadar incelenmiştir. Alt tabaka olarak, ticari fotoğraf kağıdı kullanılmıştır. Çeşitli frekans bantlarında çalışan antenler, çok seviyeli hızlı çokkutup yöntemine (MLFMA) dayalı, güçlü bir benzetim ortamında tasarlanmıştır. Antenler, standart, düşük maliyetli ve ticari yazıcılarda %25 gümüş katkılı iletken mürekkebin kullanılmasıyla basılmıştır. Basımdan sonra, gümüş mürekkep yollarının iletkenliğini artırmak için pişirme işlemi uygulanmıştır.

Dört farklı anten tipi önerilmiş ve çalışılmıştır. İlk olarak, S-monopol antenler 50 Ω giriş empedansı ve mikroçip giriş empedansı için tasarlanmıştır. Ölçüm sonuçları, 50 Ω'a uyumlu bir antenin 1.66 GHz'te -12.4 dB yansıma katsayısı ile rezonans ürettiğini göstermiştir. İkinci olarak, 50 Ω giriş empedanslı küçük (5 cm x 5.3 cm), simetrik bir dipol anten tasarlanmıştır. Bu antenin, 870 MHz'de -14 dB yansıma katsayısı ile rezonansa girdiği gözlemlenmiştir. Üçüncü olarak,

döngü-kıvrım tipi antenler ultra-yüksek frekans (UHF; 865-868 MHz) bandında radyo frekanslarında tanımlama (RFID) uygulamaları için önerilmiştir. Öncelikle, 865 MHz'te mikroçip empedansına eşlenik olarak dengelenen bir döngü anten tasarlanmıştır. Mikroçip, anten terminallerine iletken yapıştırıcı kullanılarak bağlanmıştır. Böylece, çalışan bir etiket elde edilmiştir. Daha sonra, kıvrım yapılar anten okuma mesafesini artırmak için döngü kısıma parazitik olarak eklenmiştir. Bu kapsamda, okuma mesafesi testleri için basit bir ölçüm düzeneği geliştirilmiştir. Okuma mesafesi, döngü-kıvrım anten için çıkış gücü 1 W veya 30 dBm olan 865-868 MHz bandında çalışan bir okuyucu ile ölçülmüştür. Ölçüm sonuçlarına göre, maksimum okuma mesafesi 60 cm olarak elde edilmiştir. Tez kapsamında son olarak, kafes-dipol antenler genetik algoritmalar ile tasarlanmıştır. Tasarımlar sonucu elde edilen 50 Ω uyumlu bir antenin, 1.56 GHz'te -23 dB yansıma katsayısı ile rezonansa girdiği gözlemlenmiştir. Bu anten RFID uygulamaları için 865 MHz'te rezonans üretmesi doğrultusunda yeniden tasarlanmıştır. Okuma mesafesi testleri geliştirilen düzenek ve insan bedeni üzerinde gerçekleştirilmiştir. Antenin tatmin edici şekilde, 1.5 m'den fazla mesafede ve geniş bir gözlem açısı kapsamında başarılı tanımlamalar verdiği gözlenmiştir.

Bu tez kapsamında, tasarlanan ve test edilen antenlere ek olarak, düşük-bütçeli inkjet basım adımları, inkjet basımlarda pişirme zamanı ve ısısının etkileri, ve empedans uyumluluğunun RFID antenler için önemi tartışılmıştır.

Anahtar Kelimeler: Inkjet Basım, Inkjet Antenler, Kağıt Alt Tabaka, Radyo Frekanslarında Tanımlama, Düşük-maliyetli Anten Tasarımı, İletken Gümüş Mürekkep, Okuma Mesafesi Testleri

To my dearest family...

# ACKNOWLEDGMENTS

Foremost I would first like to thank Assoc. Dr. Özgür Ergül for his supervision, guidance and suggestions throughout this thesis. My profound gratitude also goes to him for his constant support and encouragement.

I would like to thank Prof. Dr. Gülbin Dural Ünver, Prof. Dr. Gönül Turhan Sayan, Prof. Dr. Mustafa Kuzuoğlu, and Assoc. Prof. Dr. Vakur Behçet Ertürk for participating in my jury and their valuable comments.

I also thank Barışcan Karaosmanoğlu, Can Önol, Türker Dolapçı, Hande İbili and all group members of CEMMETU for their assistance during my research study.

I would like to express my gratitude to Damla Alptekin for her precious support. I would like to thank all of my friends for their support and friendship. Finally, I would like to thank my family for their everlasting support and love.

# TABLE OF CONTENTS

ABSTRACT . . . . . v

ÖZ . . . . . vii

ACKNOWLEDGMENTS . . . . . x

TABLE OF CONTENTS . . . . . xi

LIST OF TABLES . . . . . xiv

LIST OF FIGURES . . . . . xv

LIST OF ABBREVIATIONS . . . . . xxi

CHAPTERS

1 INTRODUCTION . . . . . 1

1.1 Review of Literature . . . . . 1

1.1.1 Scope of This Thesis . . . . . 8

2 RFID TECHNOLOGY . . . . . 11

2.1 Basic Components of an RFID System . . . . . 12

2.1.1 Tags . . . . . 12

2.1.2 Readers . . . . . 13

2.1.3 Controllers and the Overall RFID Systems . . 13

2.2 Parameters of RFID Systems . . . . . 14

2.3 The Reasons For Using RFID . . . . . 15

3 DESIGN STEPS OF INKJET-PRINTED ANTENNAS ON PAPER SUBSTRATE . . . . . 17

3.1 Inkjet Printing Routine . . . . . 17

3.1.1 Low-Cost Inkjet Printing Method . . . . . 17

3.1.2 Design Steps of Inkjet-Printed Antennas . . . . 18

3.2 The Importance of Curing in Inkjet Printing . . . . . 21

3.3 Dielectric Characterization of the Photograph Paper . . 22

3.4 Impedance Matching for RFID Antennas . . . . . 28

4 MAIN RESULTS AND DISCUSSIONS . . . . . 33

4.1 Introduction . . . . . 33

4.2 Design, Simulation and Measurement of S-Monopole Antennas . . . . . 33

4.2.1 Stages of the Antenna Design . . . . . 33

4.2.2 Simulation and Measurement Results . . . . . 34

4.3 A Symmetric Circular Dipole Antenna . . . . . 39

4.4 Design, Simulation and Measurement for Loop-Meander Antennas . . . . . 41

4.4.1 Design Stages of Loop Antennas . . . . . 41

4.4.2 Measurement Results for Loop-Meander Antennas 44

4.4.3 Reading Range Tests for Loop-Meander Antennas 45

4.5 Optimized Cage-Dipole Antennas . . . . . 51

4.5.1 Optimization Steps of Cage-Dipole Antennas . 52

4.5.2 Simulation and Measurement for Cage-Dipole Antennas . . . . . 56

4.6 Simulation and Reading Range Results for an Optimized RFID Cage-Dipole Antenna . . . . . 58

5 CONCLUSION AND FUTURE WORK . . . . . 69

REFERENCES . . . . . 71

# LIST OF TABLES

TABLES

Table 2.1 Comparison of the RFID Tags . . . . . 13

Table 4.1 Optimization Results for the Cage-Dipole Antennas Matching to 50 Ω . . . . . 62

# LIST OF FIGURES

FIGURES

Figure 1.1 T-match folded bow-tie RFID tag module configuration [1] . 2

Figure 1.2 Z-shaped CPW-fed printed monopole antenna [2] . . . . . 3

Figure 1.3 A temperature sensor on a paper substrate fabricated with inkjet printing [3] . . . . . 3

Figure 1.4 Silver ink based inkjet-printed text-meandered antennas [4] . 4

Figure 1.5 Inkjet-printed Vivaldi antenna on paper; front and back [5] . 4

Figure 1.6 Koch snowflake fractal antennas with Sierpinski triangles; (a) suggested Sierpinski model (b) square (c) circle [6] . . . . . 5

Figure 1.7 U-slot inkjet-printed antenna; top and bottom view [7] . . . . 6

Figure 1.8 Antenna printed on a ceramic-polymer substrate [8] . . . . . 6

Figure 1.9 a) Kapton substrate with silver ink b) FR4 with 18 $\mu m$ copper [9] 7

Figure 1.10 Fabrication process for a curved antenna on resin-coated paper substrate [10] . . . . . 7

Figure 1.11 Low-cost Koch snowflake antenna on paper substrate [11] . . 8

Figure 2.1 Working principle of passive RFID systems . . . . . 14

Figure 3.1 (a) Dimatix printer during inkjet-printing process [12], (b) Epson C88+ inkjet printer and ink cartridges, (c) silver ink and cleaning solution, (d)Matte photo paper . . . . . 19

Figure 3.2 All design steps of inkjet-printed antennas in this study . . . 21

Figure 3.3 Resistivity of a test structure before and after curing process 22

Figure 3.4 Relation of the resistance value to curing duration and temperature for the test structure in Figure 3.3 . . . . . 22

Figure 3.5 Microscope images of sample prints after curing at different temperatures . . . . . 23

Figure 3.6 Model of a 10 cm dipole on paper substrate and the corresponding model in the MOM/MLFMA environment . . . . . 24

Figure 3.7 Input impedance of a dipole antenna; (a) resistance (b) reactance [13] . . . . . 25

Figure 3.8 Measurement results for the 10 cm ($\lambda/2$) dipole antenna on paper substrate; (a) power reflection coefficient (b) input impedance 26

Figure 3.9 Simulation results for the 10 cm dipole antenna using HFSS with paper permittivity $3.5 \times (1 + i0.06)$ vs MLFMA with $\epsilon_{eff} \times (1 + i0.06)$ everywhere; (a) reflection coefficient (b) input impedance . . . 27

Figure 3.10 Simulation results for the 10 cm dipole antenna using HFSS with paper permittivity $3.5 \times (1 + i0.06)$ vs MLFMA with $\epsilon_{eff} \times (1 + i0.07)$ everywhere; (a) reflection coefficient (b) input impedance . . . 28

Figure 3.11 Simulation results for the 10 cm dipole antenna using HFSS with paper permittivity $3.5 \times (1 + i0.06)$ vs MLFMA with $\epsilon_{eff} \times (1 + i0.08)$ everywhere; (a) reflection coefficient (b) input impedance . . . 29

Figure 3.12 Simulation results for the 10 cm dipole antenna using HFSS with paper permittivity $3.5 \times (1 + i0.06)$ vs MLFMA with $\epsilon_{eff} \times (1 + i0.03)$ everywhere; (a) reflection coefficient (b) input impedance . . . 30

Figure 3.13 Simulation results of reflection coefficient for a cage-dipole antenna using HFSS with paper permittivity $3.5\times(1+i0.06)$ vs MLFMA with $1.3 \times (1 + i0.01)$ everywhere . . . . . 31

Figure 3.14 Simulation results of input impedance for a cage-dipole antenna using HFSS with paper permittivity $3.5\times(1+i0.06)$ vs MLFMA with $1.3 \times (1 + i0.01)$ everywhere . . . . . 31

Figure 3.15 Circuit model of a passive RFID tag with complex antenna and chip impedances . . . . . 32

Figure 4.1 S-monopole antenna (a) details of the original S-monopole design [2] (b) fabricated antenna using inkjet printing . . . . . 34

Figure 4.2 Simulation results for the S-monopole antenna . . . . . 35

Figure 4.3 Measurement results for the S-monopole antenna when it is matched to 50 Ω . . . . . 36

Figure 4.4 Connecting Higgs-4 IC to the designed S-monopole antenna . 36

Figure 4.5 (a) Simulation results for the RFID S-monopole antenna (b) the corresponding measurement results . . . . . 37

Figure 4.6 Places of feed points on the S-monopole design . . . . . 38

Figure 4.7 Simulation results of feed location trials for the S-monopole antenna matching to 50 Ω . . . . . 38

Figure 4.8 Current distributions for feeds 12, 13, and 14 . . . . . 39

Figure 4.9 Measurement results for changed feed point . . . . . 39

Figure 4.10 Measurement results for the S-monopole antenna with epoxy; (a) normal feed and (b) feed at 13th position . . . . . 40

Figure 4.11 Measurement results for the symmetric circular dipole antenna when it is matched to 50 Ω . . . . . 41

Figure 4.12 Loop antenna that is matched to chip impedance . . . . . 41

Figure 4.13 Measurement results of reflection coefficient and impedance of different loop antennas . . . . . 42

Figure 4.14 Reflection and measurement results of different loop trials; (a) loop-a (b) loop-b . . . . . 43

Figure 4.15 Reflection and measurement results of different loop trials; (a) loop-c (b) loop-d . . . . . 44

Figure 4.16 Reflection and measurement results of different loop trials; (a) loop-e (b) loop-f . . . . . 45

Figure 4.17 Reflection and measurement results of different loop trials; (a) loop-g (b) loop-h . . . . . 46

Figure 4.18 Reflection and measurement results of different loop trials; (a) loop-i (b) loop-j . . . . . 47

Figure 4.19 Measured reflection coefficient and impedance of loop antennas 48

Figure 4.20 Reflection and measurement results of different loop trials; (a) loop-k (b) loop-l . . . . . 49

Figure 4.21 Reflection and measurement results of different loop trials; (a) loop-m (b) loop-n . . . . . 50

Figure 4.22 Reflection and measurement results of different loop trials; (a) loop-o (b) loop-p . . . . . 51

Figure 4.23 Reflection and measurement results of different loop trials; (a) loop-q (b) loop-r . . . . . 52

Figure 4.24 Effects of the parasitic meander part . . . . . 53

Figure 4.25 (a) Further measurements with the loop and meander antennas, (b) effect of the loop size . . . . . 54

Figure 4.26 Measurement results for loop-meander antennas; (a) power reflection coefficient (b) input impedance . . . . . 55

Figure 4.27 Comparison of physical pressure connection and epoxy connection for loop-meander antennas . . . . . 56

Figure 4.28 Measurement results of input impedance obtained by using epoxy to attach the connector to the loop-meander antennas . . . . 56

Figure 4.29 Measurement results of reflection coefficient obtained by using epoxy to attach the connector to the loop-meander antennas . . . . 57

Figure 4.30 Mean measurement results for loop-meander antennas using epoxy in measurements . . . . . 57

Figure 4.31 Measurement results for loop-meander antennas with different number of turns . . . . . 58

Figure 4.32 Effect of parasitic parts on the reading range . . . . . 58

Figure 4.33 (a) Rotation tests for the 6-turn loop-meander antenna, (b) range values . . . . . 59

Figure 4.34 Reading tests on foam for the 6-turn loop-meander antenna . 59

Figure 4.35 Reading tests on foam with fractal parasitic element . . . . . 60

Figure 4.36 Reading ranges for the 6-turn loop-meander antenna when it is placed on different materials . . . . . 60

Figure 4.37 Reading range of antennas on human body at two different positions . . . . . 61

Figure 4.38 Geometry of cage-dipole antennas and gap locations. An optimized configuration is shown. Green and red colors represent short circuit (no gap) and open circuit (gap), respectively. . . . . 61

Figure 4.39 Current distributions on the cage-dipole antenna excited by 1V delta-gap source (a) computational gaps (b) modeled gaps . . . . 62

Figure 4.40 Radiation patterns of the cage-dipole antenna excited by 1V delta-gap source; using (a) computational gaps (b) modeled gaps . . 63

Figure 4.41 Measurement setup of the optimized cage-dipole antenna that is attached to a coaxial end with physical press . . . . . 63

Figure 4.42 Simulation and measurement results for the optimized cage-dipole antenna from 1 GHz to 4 GHz . . . . . 64

Figure 4.43 Simulation results of power reflection coefficient and input impedance of the RFID cage-dipole antenna from 0.3 GHz to 7 GHz 64

Figure 4.44 Power reflection coefficient results for the RFID cage-dipole antenna from 0.3 GHz to 7 GHz using calculated and modeled gaps 65

Figure 4.45 Power reflection coefficient and input impedance of the RFID cage-dipole antenna from 0.3 GHz to 2 GHz using computational and modeled gaps . . . . . 65

Figure 4.46 Power reflection coefficients for the 4.7 cm (width) RFID cage-dipole antenna from 0.3 GHz to 2 GHz using computational and modeled gaps . . . . . 66

Figure 4.47 Reading range values for the optimized cage-dipole antenna obtained via measurements . . . . . 66

Figure 4.48 Reading range of the optimized RFID cage-dipole antenna on human body . . . . . 67

# LIST OF ABBREVIATIONS

| | |
|---|---|
| AIDC | Automatic Identification and Data Capture |
| AUTO-ID | Automatic Identification |
| CPW | Coplanar Waveguide |
| EFIE | Electric-Field Integral Equation |
| ETSI | European Telecommunications Standards Institute |
| GA | Genetic Algorithm |
| GPS | Global Positioning System |
| HF | High Frequency |
| HFSS | High Frequency Structure Simulator |
| IC | Integrated Circuit |
| LF | Low Frequency |
| MLA | Meander Line Antenna |
| MLFMA | Multilevel Fast Multipole Algorithm |
| OCR | Optical Character Recognition |
| PCB | Printed Circuit Board |
| RF | Radio Frequency |
| RFID | Radio Frequency Identification |
| SMA | Sub Miniature Version A |
| UHF | Ultra High Frequency |
| UWB | Ultra Wideband |
| VSWR | Voltage Standing Wave Ratio |
| WSN | Wireless Sensor Networks |
| WLAN | Wireless Local Area Network |

# CHAPTER 1

# INTRODUCTION

Inkjet printing is a relatively new technology involving liquid droplets that are jetted directly onto a substrate for patterning [9]. It is an inexpensive, environmentally-friendly, and direct write method. In addition, inkjet-printed antennas are convenient to be produced with flexible substrates such as paper, Kapton, and silicone. Traditionally, printed circuit board (PCB) processes, called subtractive methods, are used for antenna production. These methods are both cost and time inefficient since they involve a lot of different processes such as masking and etching operation. To overcome these problems, inkjet-printed antennas on flexible substrates are suggested [1], where inkjet-printed ultra-high frequency (UHF) and microwave circuits fabricated on paper substrates are investigated for the first time.

Inkjet printing method can be used for various applications, such as pharmaceutics and biomedical engineering, optics, and micro-electronics. This method is especially compatible with radio frequency identification (RFID) applications. Practical implementations of RFID applications must be inexpensive, compact, low-profile, useful, robust, and available on demand [14]. Inkjet printed antennas on paper substrates can fulfil these requirements.

## 1.1 Review of Literature

A review of studies on inkjet-printed antennas on flexible substrates and related topics are summarized as follows.

As one of the first studies, Yang et al. [1] studied RFID tags and different RF structures on paper substrates using inkjet printing technology. An RFID antenna was fabricated for the UHF frequency band, and multilayer RF structures were explored. Low-cost inkjet printing techniques, as well as effects of temperature on silver ink were investigated. It was shown that different temperature levels affect the conductivity of silver paths. A copper-metalized antenna was printed and compared to the inkjet-printed antenna. It was demonstrated that the return loss of the inkjet-printed antenna was larger than the copper one. RFID tag design was realized with T-match folded bow-tie antenna, as shown in Figure 1.1 [1].

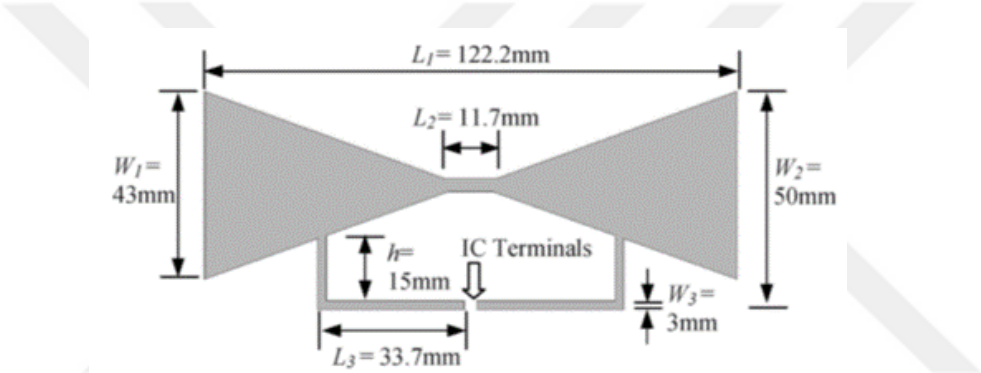



Figure 1.1: T-match folded bow-tie RFID tag module configuration [1]

Konstas et al. [2] designed a Z-shaped monopole antenna on paper substrates using inkjet printing. In this paper, a coplanar waveguide (CPW) fed monopole antenna was proposed; advantages of the ground plane in matching, sensors and broadcast characteristics were explained. It was shown that microchip impedance changes with frequency. The proposed Z-shaped antenna, which is also shown in Figure 1.2, was operating in the UHF band and it was fabricated with Dimatix DMP-2800 printer. In addition to the previous paper, an adhesive silver epoxy was used to measure the antenna with sub miniature version A (SMA) connector. This material was preferred for better connections between the paper substrate and the connector [2].

In 2009, Rida et al. [3] proposed flexible, low-cost antennas on paper substrates

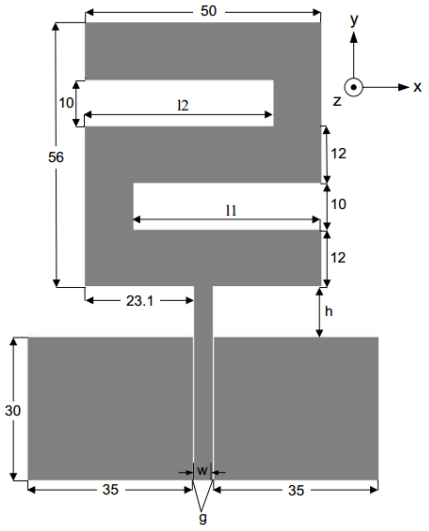



Figure 1.2: Z-shaped CPW-fed printed monopole antenna [2]

for RFID in UHF and wireless sensor network (WSN) applications. In this study, dielectric behavior of paper was analyzed. The main contribution of this paper was inkjet-printed antennas that can work with sensor networks. A Dimatix DMP-2800 printer with DMC-11610 cartridge (drop volume of 10 pL) was used to print the antennas. The thickness of silver ink traces were nearly 25 $\mu m$. A folded bowtie RFID antenna combined with a T-match circuit was developed, as shown in Figure 1.3. The impedance measurement was conducted using a GS1000 $\mu m$ pitch probe. This was the first time that a full sensor was attached to an inkjet-printed antenna, all on paper substrates [3].

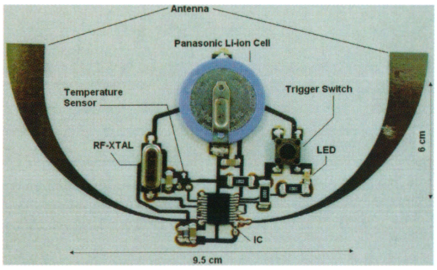



Figure 1.3: A temperature sensor on a paper substrate fabricated with inkjet printing [3]

Marroncelli, Trinchero, and Tentzeris [4] contributed to inkjet-printed technol-

ogy with text-meandered antennas, which involve letters as meander traces. Silver-based conductive ink was used to print samples. An example to a meander line antenna involving some letters can be seen in Figure 1.4. Letters can be brought up as radiating elements, therefore manufacturer logos and pictures can also be produced as antennas [4].




Figure 1.4: Silver ink based inkjet-printed text-meandered antennas [4]

The antenna proposed by Cook and Shamim [5] can be considered as an example of high-gain, wideband inkjet antennas. Laser curing was introduced for the first time in this work. Laser curing and heat sintering methods were compared. Antenna resistance as a function of heating duration between $120°C$ and $200°C$ was presented. The required conductivity was reached in thirty minutes at $200°C$. On the other hand, the same results were achieved in a few seconds with laser sintering using less power consumption. Wideband inkjet-printed Vivaldi antennas were studied with simulation and measurement results (see Figure 1.5).

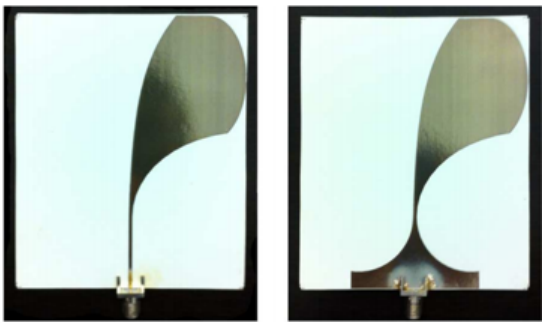


Figure 1.5: Inkjet-printed Vivaldi antenna on paper; front and back [5]

Similarly, Maza et al. [6] studied inkjet-printed ultra wide-band fractal antennas.

The article included a Koch Snowflake monopole fractal antenna associated with Sierpinski triangles. Sample antennas can be observed in Figure 1.6. Some parts of the antennas were removed in order to extend impedance bandwidth [6].

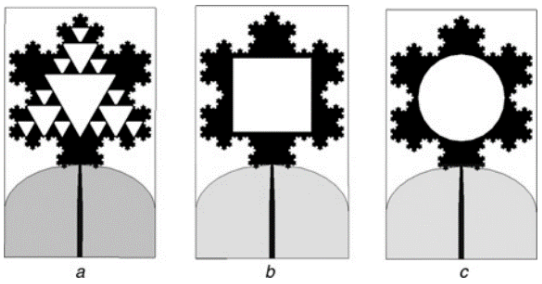



Figure 1.6: Koch snowflake fractal antennas with Sierpinski triangles; (a) suggested Sierpinski model (b) square (c) circle [6]

An inkjet-printed antenna on paper substrate was adapted for multiband operations for the first time by Abutarboush and Shamim [7]. A monopole antenna with U-shaped slots was designed to involve WIMAX, wireless local area network (WLAN), and global positioning system (GPS) frequencies. The monopole antenna consisted of a ground plane, rectangular radiator, and 50 Ω feed line. U-slots in the main radiation body of the antenna ensured high bandwidth and tri-band operation, without changing the antenna size. The whole proposed antenna operated at around 1.57 GHz, 3 GHz, 5 GHz, and can be seen in Figure 1.7. Ground plane of the antenna was printed on a paper, while feed line and radiator were printed on another paper. Both layer were glued to obtain the overall structure [7].

Inkjet-printed UHF RFID antenna on flexible ceramic-polymer composite substrate was demonstrated in [8]. This paper was an instance for using different substrates in inkjet-printed antennas. Ceramic polymer substrate is hydrophobic, flexible material that has high permittivity, allowing smaller antenna sizes. An integrated circuit (IC) microchip was connected to the antenna ports using silver epoxy (see Figure 1.8).

A folded dipole antenna was designed for remote sensing in UHF band in [15]. A

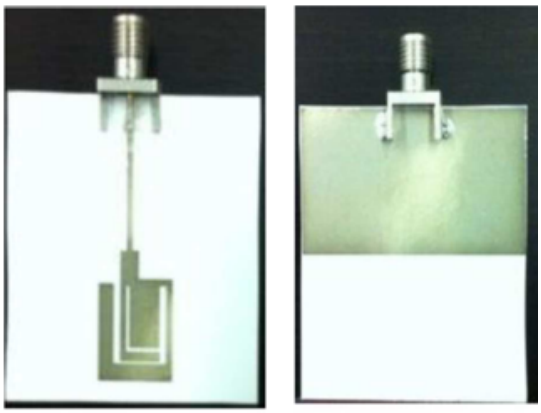



Figure 1.7: U-slot inkjet-printed antenna; top and bottom view [7]

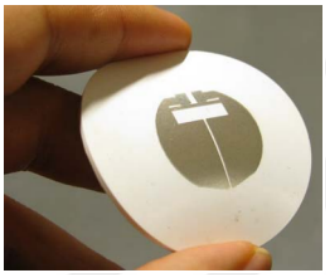


Figure 1.8: Antenna printed on a ceramic-polymer substrate [8]

microchip was attached to the antenna to communicate with the RFID reader. Threshold power formula for starting up the chip was given when the antenna was printed on paper substrate [15].

Printed antennas on copper substrates and inkjet-printed antennas on different substrates using conductive silver ink were fabricated and compared in [9]. The selected substrates were FR4 laminate, PET, and Kapton. Copper antenna was fabricated on FR4, while inkjet-printed antennas were produced on PET and Kapton substrates. Silver inkjet-printed antennas had high resistances. Therefore, they led to shorter ranges than the antenna produced on FR4 with copper paths. Nevertheless, the ranges of inkjet-printed antennas were more than sufficient. The antennas that were printed using silver ink on Kapton and using copper on a FR4 substrate are shown in Figure 1.9 [9].

A foldable inkjet-printed antenna on paper substrate was presented for multi-band operations in [10]. This monopole antenna was fabricated on resin-coated




Figure 1.9: a) Kapton substrate with silver ink b) FR4 with 18 $\mu m$ copper [9]

paper which allows foldable, curved flexible antennas. The antenna was fed by 50 $\Omega$ microstrip line and it consisted of four lines, three L-slots ground (see Figure 1.10) [10].




Figure 1.10: Fabrication process for a curved antenna on resin-coated paper substrate [10]

Problems that are faced during the fabrication of low-cost inkjet-printed paper antennas were summarized at [16]. Commercial desktop printers with silver based cartridges were used for printing antennas in this study. Principal parameters were listed as printer type, ink type (silver ratio of ink), paper size and type, curing temperature and time, and connector challenges. The antennas were designed for RFID applications, where complex chip impedance values appear as major issues. It was also shown that standard printers may cause consistency problems while measuring the antennas, i.e., results can change for different trials of the identical antennas. It was stated that, despite many challenges in design and production, very low-cost inkjet antennas can be realized.

Advantages of low-cost inkjet printing using an ordinary desktop printer was discussed in [11]. Design, simulation, production, and measurement steps were explained. In these studies, the multilevel fast multipole algorithm (MLFMA)

in frequency domain was used as the simulation tool [17]. In addition, the electric-field integral equation (EFIE) was used in the three-dimensional space for modeling antennas. A Koch snowflake multiband antenna was realized and measurements were conducted for the frequency band from 500 MHz to 9 GHz. This design is shown in Figure 1.11.



Figure 1.11: Low-cost Koch snowflake antenna on paper substrate [11]

### 1.1.1 Scope of This Thesis

The objective of this thesis is to realize the low-cost inkjet printing method for different types of antennas on photograph paper substrate. This study utilizes cost-effective inkjet printing using standard printers, commercial oven, and commercial photo paper. The antennas are particularly designed for the RFID-UHF frequency bands. In addition, reading range measurements are carried out on the designed antennas. The thesis is organized into five chapters, as follows.

In Chapter 2, RFID technology is investigated in detail. Basic components of the RFID system, especially the concept of passive tag is presented. The reasons for using RFID in different application areas are discussed.

In Chapter 3, the developed inkjet printing routine is presented step by step. Low-cost, fast, direct-write printing procedures are explained in detail. The designed inkjet printing method for fabricating the antennas and its advantages are demonstrated. Dielectric characterization of the used photo paper is also

shown. Finally, impedance matching procedure is explained.

In Chapter 4, designed and fabricated antennas using the inkjet printing technology are presented. Four different antenna types are investigated in this chapter: S-monopole antennas, symmetric dipole antennas, loop-meander antennas, and cage-dipole antennas. These antennas are designed for 50 Ω input impedance, as well as for and RFID-compatible input impedances. Experimental results are presented for the return loss and input impedance measurements, in addition to the reading range tests for RFID antennas.

Chapter 5 summarizes the whole study and highlights the future work.

# CHAPTER 2

# RFID TECHNOLOGY

Automatic identification and data capture (AIDC) is a technology, involving automatic identification of objects, collection and transfer of the produced information directly to the computer systems without human activity. In AIDC systems, data is mainly processed by the computer systems. Accuracy and efficiency of the system can be increased and data errors can be reduced by automated identification [14]. Barcodes, RFID, optical character recognition (OCR), smart cards and biometric iris recognition can be listed under the existing automatic identification (AUTO-ID) technologies [18].

RFID is a kind of AUTO-ID technology based on the identification and track of objects using electromagnetic waves. Specifically, most RFID systems use electromagnetic waves for constructing a communication link between the reader and the tag. Identification information is stored in an IC microchip and detected by a reader. There is no need for direct contact or line-of-sight monitoring in major RFID systems. This feature is the advantage of RFID compared to other identification technologies [18], [19]. As the fabrication costs of RFID tags are reduced, RFID applications increasingly become popular in many different areas, such as access control, asset tracking, livestock tracking, security, delivery, and logistics systems [3], [20].

## 2.1 Basic Components of an RFID System

RFID systems are typically composed of three basic elements: Tags, readers, and the computer system. These components are now explained in detail.

### 2.1.1 Tags

An RFID tag consists of an antenna and an IC microchip attached to or mounted on the antenna [21]. RFID tags can be categorized as active tags, semi-active tags, and passive tags, depending on their power supply position [18].

An active tag has an internal power supply, which is generally a battery. Active tags periodically transmit the ID signal. The power source is used to run the circuits of the microchip and transmit signals to the reader. Therefore, active RFID tags do not need any energy from the reader to send the ID information. On the other hand, passive RFID tags have no internal battery; power is supplied by the reader. RF energy is used to activate the microchip circuits and set up a communication between the tag and the reader. Working procedure of a typical passive RFID system has two steps as follows: The reader broadcasts the power and passive tag gets this power to activate the microchip. After the chip is activated, identification data is sent back to the reader with the help of the tag antenna. Semi-passive tags can be described as battery-operated passive tags. The working principles of semi-passive tags is similar to the passive tags, but the main difference is that semi-passive tags have an internal power supply. This on-board battery is used to activate the integrated circuits for producing a response to the reader. Sensors can be activated with this internal power.

The advantages and the disadvantages of RFID tags are listed in Table 2.1. In our applications, the passive tags are preferred since they are inexpensive and smaller than the other tags. In addition, they are suitable to produce on paper substrates.

Table2.1: Comparison of the RFID Tags

| Tag | Advantages | Disadvantages |
|---|---|---|
| Active | Long read range ($\sim$ 30 m). Sensors can be activated through the internal battery. | Expensive. Physically larger (limited applications). |
| Passive | Lifetime is long. Light, small, and inexpensive. | Relatively short read range. Not suitable as sensors. |
| Semi Passive | Long read range in comparison to passive tags. | Shorter life due to battery. |

### 2.1.2 Readers

An RFID reader consists of a transceiver antenna, an RF electronics module, and a controller module. Such a reader generally works as a bridge between the RFID tag and the controller. When a tagged object enters into the read zone or when the user activates the reader the reader transmits the activation energy. The main functions of RFID readers can be listed as follows: Providing power to activate passive tags, reading data from RFID tags, and transmitting data to controllers. Other important functions are data encryption, protecting the integrity of data, preventing the unauthorized access via identity check. ATiD870 hand held UHF RFID reader is used in our applications, as shown in Figure 2.1.

### 2.1.3 Controllers and the Overall RFID Systems

In RFID systems, controllers usually consist of computer systems. Computer systems process the data transmitted by the reader, and they run database structures for processing and interpretting the data [22].

As a brief summary, working principle of a passive RFID system, as a major focus of this thesis, is shown in Figure 2.1. A reader broadcasts a modulated signal and this type of transmission is called downlink. This RF signal is received by the passive tags. The tags are also powered with the received energy. In a passive tag, IC microchip is activated by the received signal. Modulated carrier

signal is transmitted back by the tag antenna, which is called uplink. Reader antennas receive the returned signal. The reader decodes the signal into digital data and send to the controller [18].




Figure 2.1: Working principle of passive RFID systems

## 2.2 Parameters of RFID Systems

RFID systems can be integrated into a wide range of applications. In general, reading range requirements change for application types. Specifically, preserving the desired read range is always the most important issue in RFID systems. From this perspective, RF power output, sensitivity of the reader, and module size affect the performance of the system. Hence, selecting the right choices for the designed system is of utmost importance. Some important parameters are as follows.

• **Operating Frequency**: Operating frequency of the reader is an important parameter for an RFID system. Tag characteristics fully depend on the working frequencies of the tag antennas. RFID devices can be fabricated in different transmission frequencies ranging from 135 kHz to 5.8 GHz. Low-frequency (LF) tags operate in 125 KHz to 134 KHz band. These tags have short read range of 10 cm and slower read speed; therefore, they are often used for animal tracking and security systems. High-frequency (HF) tags operate at 13.56 MHz. Fabrication of HF tags is cheaper and easier than LF tags. They have higher data rates and typically 30 cm - 1 m read range. HF RFID is preferred for ticketing, payment, and data transfer applications [18]. UHF tags have even faster data rates than

LF and HF tags. The read range of passive UHF systems can be as long as decades of meters. In addition, fabrication of UHF tags is easier and cheaper. In this study, tags and readers are selected to operate in the UHF band (865-868 MHz).

• **Range**: The read ranges depend on the type of the application. The distances above 1 m are accepted as long ranges. All long-range systems operate using electromagnetic waves in the UHF band and even at microwave frequencies. Transmission frequency, gain of the reader antenna and tag antenna, polarization, orientation, size, and placement of the tag, power of the reader, whether the tags active or passive, and many other environmental factors affect the read-range performance [20]. In our study, the maximum read range is obtained as 2 m - 3 m.

• **Tag Size**: Application area is the main factor that determines the size of the tag. For example, for the airline baggage strips and identification cards, tags must be small enough to fit into compact objects [20]. Identification cards for access control are mainly considered in our applications. Among various dimensions that are suitable for such applications, the smallest size of an RFID tag is obtained as 5.4 cm $\times$ 2.1 cm.

## 2.3 The Reasons For Using RFID

The advantages of RFID systems can be listed as follows.

• No Need For Line of Sight: RFID tags do not need line of sight for reading information up to the range of a few meters. This is the advantage of RFID products compared to the barcode systems [23].

• Robustness: Some RFID systems are designed to resist hard conditions, such as harsh and liquid environments.

• Read Speed: RFID systems are especially useful for identifying objects that are moving quickly, like those in a production line.

• Multiple Interaction: More than one tags can be read at the same time with most RFID readers.

• Security: Tags are programmed with a unique serial identification. This identification number provides a guarantee for the tag to be unique throughout the world.

• Programmability: Many chips are not only readable but also writable [18].

# CHAPTER 3

# DESIGN STEPS OF INKJET-PRINTED ANTENNAS ON PAPER SUBSTRATE

## 3.1 Inkjet Printing Routine

In inkjet printing process, droplets of conductive ink are propelled onto a substrate. Voltage is applied to piezoelectric stripes and an actuator changes head's volume. This creates a pressure wave in the fluid ink drops. Positive pressure waves cause that ink droplets are pushed out from the nozzles onto the substrate directly [24, 25].

### 3.1.1 Low-Cost Inkjet Printing Method

This thesis demonstrates different examples of inkjet-printed antennas produced by using conductive silver ink on photograph paper substrates. There are different types of printers for the inkjet printing antennas. Dimatix printers, which are widely used in the recent literature, can be seen in Figure 3.1 (a). These printers are specifically used for material printing, including silver-based inks. However, in this study, commercially available Epson Stylus C88+ Color is used for printing. Actually, this is a normal type of printer which is not specialized for material printing. In our applications, the ink cartridges that come with the printer are removed. Instead, inkjet cartridges that are filled with conductive silver-based ink are inserted into the printer. As the conductive ink, 25% silver alloyed ink that is produced by Novacentrix with Metalon JS-B25P model

number is used (see Figure 3.1 (c)). Even though Epson C88+ inkjet printers are commercial and inexpensive, they have good resolution and can print uniform images. The minimum ink trace is defined as 0.2 mm. The printer and cartridges, which are used in this thesis and also shown in Figure 3.1 (b), cost less than $100. Using an inexpensive setup, the nozzles of the printer must be cleaned out after each printing. Cleaning solution is depicted in Figure 3.1 (c) along with silver conductive ink.

Inkjet printing routine with Epson C88+ can be summarized by the following steps.

• Computer is connected to the printer and inkjet cartridges are installed. The cartridges are filled with Metalon JS-B525P conductive silver ink shown in Figure 3.1 (c).

• Nozzles are controlled and the nozzle heads are cleaned if they are clogged.

• In the printer settings, quality option is chosen as 'Best Photo' and the paper type is chosen as 'Matte Paper'.

• The drawn antenna in black color on computer is printed, as usual, similar to printing a normal picture.

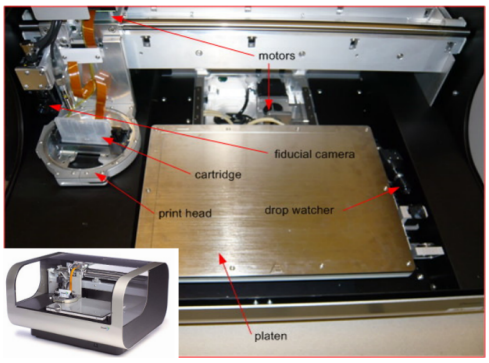
• After a printing session, the nozzle heads must be cleaned again to avoid clogging.

### 3.1.2 Design Steps of Inkjet-Printed Antennas

Design steps of inkjet antennas can be listed as follows.

1. Antenna geometry is drawn using Siemens NX software, which also discretizes the geometry using triangular meshes.

2. Drawn antenna is converted to a model file and simulated via a full-wave solver based on MLFMA in frequency domain. Antenna surfaces are formulated using EFIE [17].




(a)




(b)




(c) (d)

Figure 3.1: (a) Dimatix printer during inkjet-printing process [12], (b) Epson C88+ inkjet printer and ink cartridges, (c) silver ink and cleaning solution, (d)Matte photo paper

3. After the design process involving cycles of items 1 and 2, the black copy of the final antenna is generated and printed on photograph papers as de-

scribed above. Canon inkjet GP-501 photo paper with thickness of 0.254 mm is used as substrate. We usually print more than one samples simultaneously.

4. Immediately after the printing, the antennas must be cured. In this step, commercially available oven is used for curing. Antennas are kept in oven at $160°C$ -$170°C$ for around 90 minutes. Temperature and duration of curing have remarkable roles to get highly conductive ink paths that are crucial for the efficiency of the antenna.

5. For the measurement of a cured sample, the antenna is combined with a connector that is compatible with the network analyzer. We use a standard SMA connector for this purpose. To attach SMA connector to the paper substrate and the antenna, two methods are used. The first method is a physical pressure, in which the connector is attached to the terminals of the antenna by physically inserting some buffer paper behind the connector. The second method is using a conductive epoxy. We use a type of epoxy, namely EPO-TEK H20E 1OZ Kit, which is a silver-doped adhesive material. Using epoxy, second heat sintering is needed for around 20 minutes at $80°C$.

6. After the connection to SMA, reflection coefficient and input impedance values of the antenna are measured via network analyzer. The input impedance of the antennas are extracted from the measured reflection coefficient or obtained directly from the Smith Chart. These values are substituted in the power reflection coefficient equation.

7. Measurement results are compared with simulation results. If the results are consistent with each other, field tests can be realized, otherwise the designs may need to be modified (e.g., scaling may be applied) [11].

Design, simulation, fabrication, printing, curing, and measurement steps can be seen in Figure 3.2.

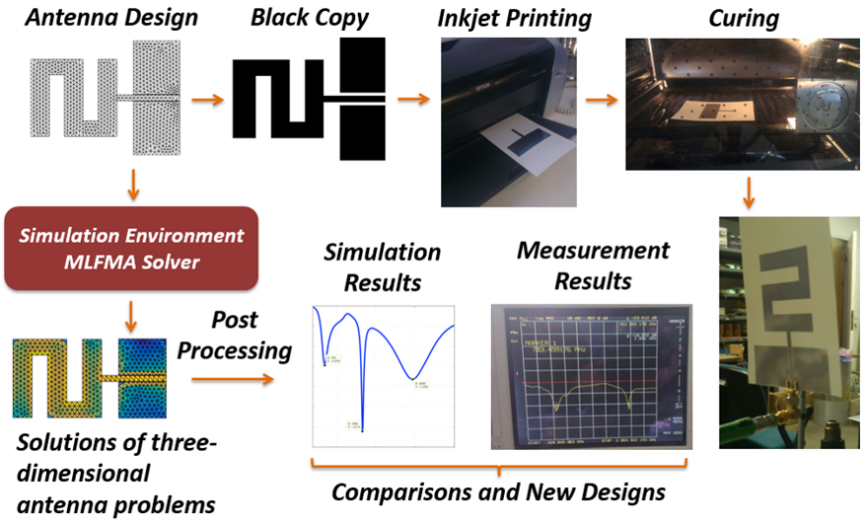



Figure 3.2: All design steps of inkjet-printed antennas in this study

## 3.2 The Importance of Curing in Inkjet Printing

Immediately after printing, curing process is applied to increase the conductivity of silver ink traces. Metallic nanoparticles of silver based ink are usually covered by a polymer film to protect the fluid structure of the ink. With heat sintering, the polymer film can be disposed and melted [5], leaving only ink on the paper.

In commercial printers, an important property is the resolution of images. However, for inkjet printing, uniformity becomes more crucial. Curing process also improves the uniformity.

Our experiments show that duration and temperature of curing directly determine the resistance of the prints. For example, usually resistance of a long strip is tens of $k\Omega$ immediately after the printing, whereas it becomes a few $\Omega$ after a curing for 1 hour at $160°C-170°C$. Figure 3.3 shows the resistance values of a test structure before and after the curing. The resistance of the silver ink trace is measured as 12 k$\Omega$ and 60 $\Omega$ before and after the curing, respectively.

The relation between the resistance and the curing duration for different temperatures is shown in Figure 3.4. As seen from the graph, increasing the curing time helps to decrease the resistance. However, for reasonable durations, temperature must be high enough. Increasing the temperature too much has negative

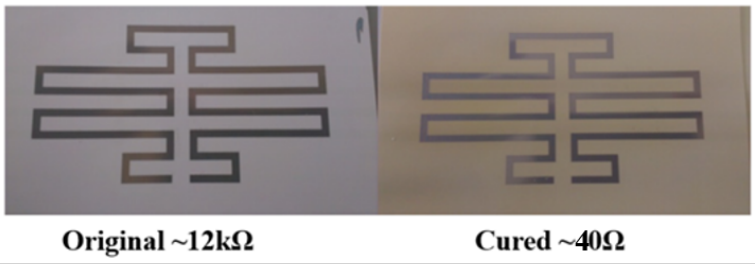



Figure 3.3: Resistivity of a test structure before and after curing process

effects, such as bents and cracks on the print. Therefore, there is an optimal level of temperature, i.e., around $160°C$. Microscope images are further used to observe the effect of the temperature as shown in Figure 3.5. It is seen that, as the curing temperature increases, conductive silver traces become more denser, leading to better conductivity.

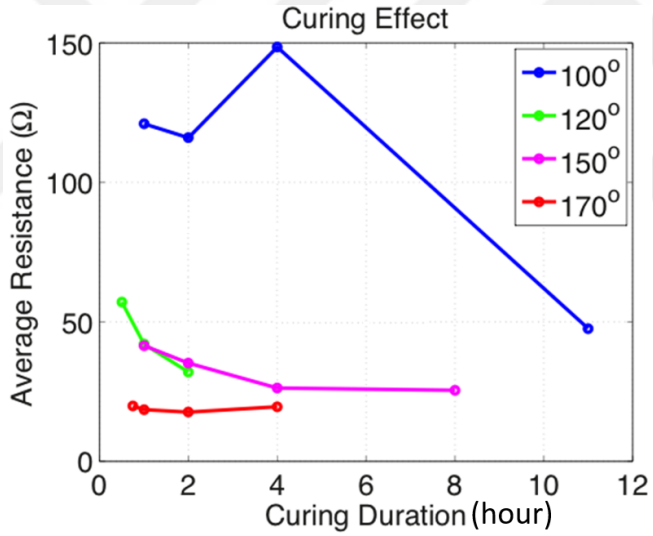



Figure 3.4: Relation of the resistance value to curing duration and temperature for the test structure in Figure 3.3

## 3.3 Dielectric Characterization of the Photograph Paper

As mentioned before, standard photograph paper is used as substrate in this work. For accurate simulations, electrical properties of the used paper should

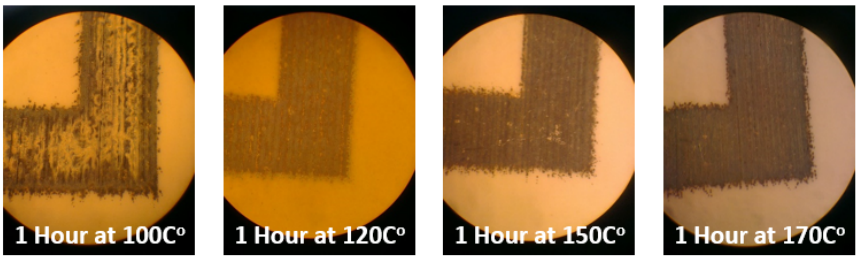



Figure 3.5: Microscope images of sample prints after curing at different temperatures

be known. Since a commercial type photograph paper is used instead of well-known microwave substrates, its electrical properties are not available [5], [12].

In this study, Canon GP-501 glossy inkjet photo paper is used for printing the antennas. The overall size of each paper is 10 cm (width) × 15 cm (length) × 0.0254 cm (thickness). The permittivity $\epsilon$ of a linear, homogeneous and isotropic medium is in general a complex quantity and expressed as $\epsilon = \epsilon_0\epsilon_r = \epsilon_0(\epsilon'_r + i\epsilon''_r)$, where $\epsilon_0$ is the permittivity of vacuum and $\epsilon_r$ is the relative permittivity. Permittivity expression can be written in terms of $tan\delta$ as $\epsilon = \epsilon_0\epsilon'_r(1+i(\frac{\epsilon''_r}{\epsilon'_r})) = \epsilon_0\epsilon_r \times (1 + itan\delta)$.

The MLFMA/MOM simulation environment used in this work assumes material in the entire surrounding medium. The effective permittivity of the host medium is set in MOM/MLFMA as $\epsilon_{eff}\times(1+itan\delta)$, where $\epsilon_{eff}$ and $tan\delta$ must be known. In Figure 3.6, a 10 cm ($\lambda/2$) dipole is shown on paper substrate, where the dipole is modeled in the MOM/MLFMA environment in a surrounding medium with $\epsilon_{eff}$. Effective permittivity ($\epsilon_{eff}$) and loss tangent ($tan\delta$) values can be found iteratively using such a structure that has known solutions. The input impedance of a dipole antenna is well defined; general formulations are found for a small thin dipole antenna in [13]. Specifically, the input resistance and input reactance are given as $R_{in} = \left(\frac{I_0}{I_{in}}\right)^2 R_r$ and $X_{in} = \left(\frac{I_0}{I_{in}}\right)^2 X_m$, where $R_{in}$ is the radiation resistance at input(feed) terminals, $R_r$ is the radiation resistance at current maximum, $I_0$ is the current maximum, and $I_{in}$ is the current at input terminals. For a dipole of length $l$, current at input terminals is defined as $I_{in} = I_0 sin(\frac{kl}{2})$ and the input resistance and input reactance can be written as

$R_{in} = \frac{R_r}{sin^2(\frac{kl}{2})}$ and $X_{in} = \frac{X_m}{sin^2(\frac{kl}{2})}$. Calculated input resistance and reactance values using these formulas are depicted in Figure 3.7 for the dipole length of $0 \leq l \leq 3\lambda$ and a dipole radius of $10^{-5}\lambda$ [13]. As a comparison, a 10 cm ($\lambda/2$) dipole is printed on paper substrate and measured, as presented in Figure 3.8.

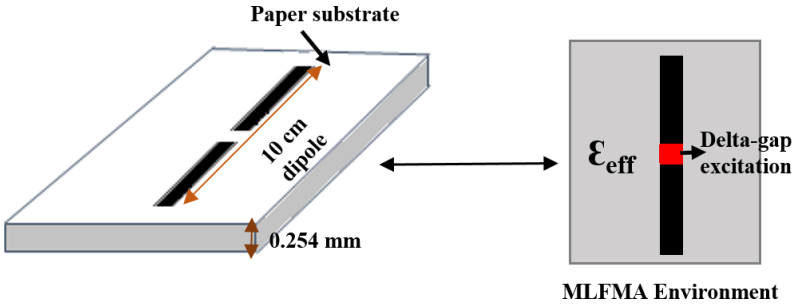
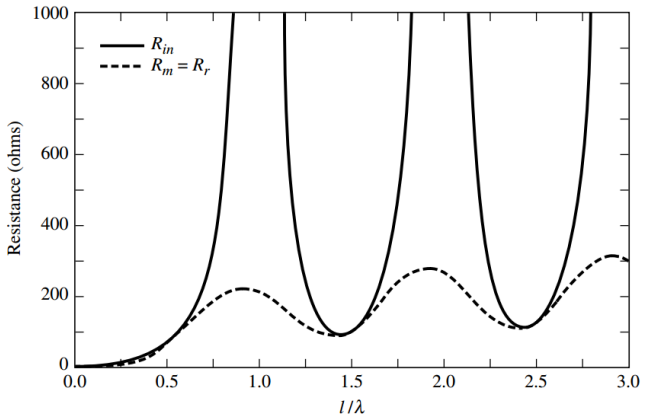



Figure 3.6: Model of a 10 cm dipole on paper substrate and the corresponding model in the MOM/MLFMA environment

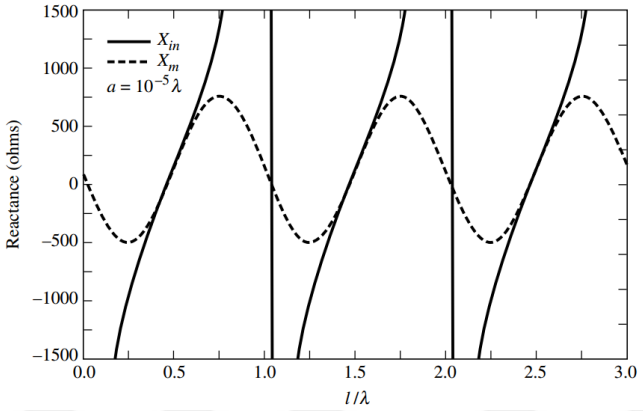
In order to find effective medium parameters, the 10 cm dipole antenna is simulated in the MOM/MLFMA environment from 300 MHz to 6 GHz with 50 MHz steps. Delta-gap source is used for the excitation of the antennas. The effective permittivity of the surrounding medium is changed parametrically for different tangent loss ($tan\delta$) values. In addition, a reference simulation result is extracted using ANSYS High-Frequency Structure Simulator (HFSS) software.

The power reflection coefficient and input impedance values for MOM/MLFMA and HFSS simulations are given in Figure 3.9. In these results, the effective permittivity of the surrounding medium is set in MOM/MLFMA as $\epsilon_{eff} \times (1 + i0.06)$ where $\epsilon_{eff}$ changes from 1.0 to 1.5. Whereas, in HFSS, permittivity of the substrate is assigned as $3.5 \times (1 + i0.06)$. This value is the closest one to the measurement and semi-analytical results. It is observed that MLFMA becomes consistent to HFSS when $\epsilon_{eff} = 1.2$ is chosen.

Different $tan\delta$ values are further considered to observe the effect of the loss on the resonance frequency and the magnitude of the power reflection coefficient. The power reflection coefficient and input impedance values for MOM/MLFMA and HFSS simulations are presented in Figure 3.10 and Figure 3.11. Once again,




(a)

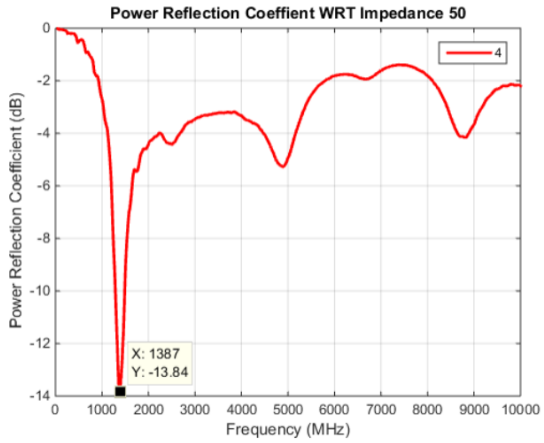



(b)

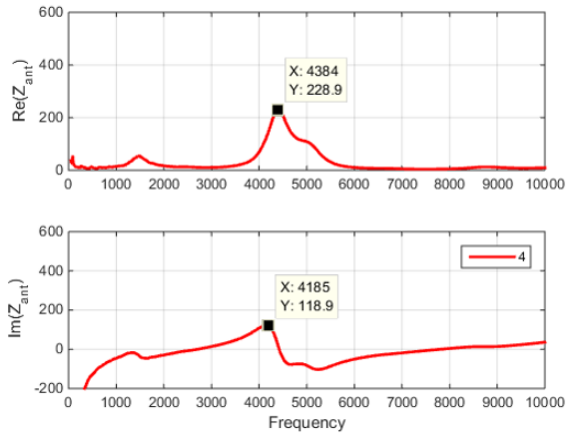
Figure 3.7: Input impedance of a dipole antenna; (a) resistance (b) reactance [13]

the effective permittivity of the surrounding medium is set in MOM/MLFMA as $\epsilon_{eff} \times (1 + itan\delta)$ where $tan\delta$ is 0.07 and 0.08, respectively.

By increasing the tangent loss value, it is observed that there is no significant change in the resonance frequency. When the $tan\delta$ values are compared, dip values reach the most consistent values for $tan\delta = 0.06$. Considering numerical results and performing numerous numerical simulations and comparisons, the final power reflection coefficient and input impedance values for MOM/MLFMA and HFSS simulations are given in Figure 3.12. In this figure, the effective permittivity of the surrounding medium is set in MOM/MLFMA as $\epsilon_{eff} \times (1 + i0.03)$ where $\epsilon_{eff}$ changes from 1.15 to 1.19, while $tan\delta = 0.03$. According to the simulation results, the best fit values of the effective permittivity of the




(a)

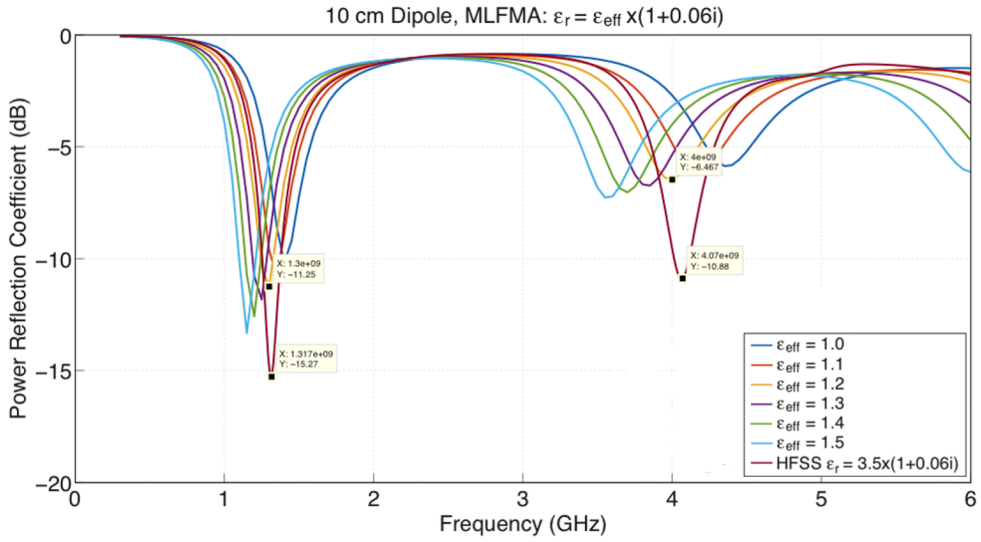



(b)

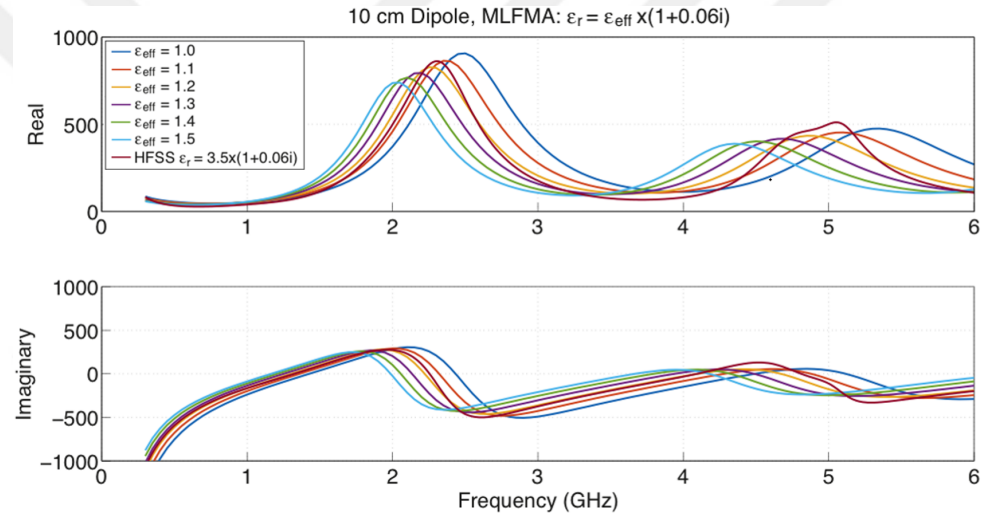
Figure 3.8: Measurement results for the 10 cm ($\lambda/2$) dipole antenna on paper substrate; (a) power reflection coefficient (b) input impedance

surrounding medium is found as $1.17 \times (1 + i0.03)$.

Effective permittivity values found for an antenna can be used for a large class of antennas with similar geometries. On the other hand, the procedure described above must be repeated for significantly different geometries. For example, a cage dipole antenna is simulated in HFSS by setting the permittivity of the paper substrate as $3.5 \times (1 + i0.06)$. The power reflection coefficient and input impedance values for the cage dipole found by MOM/MLFMA and HFSS simulations are compared in Figure 3.13, 3.14. Once again, the effective permittivity



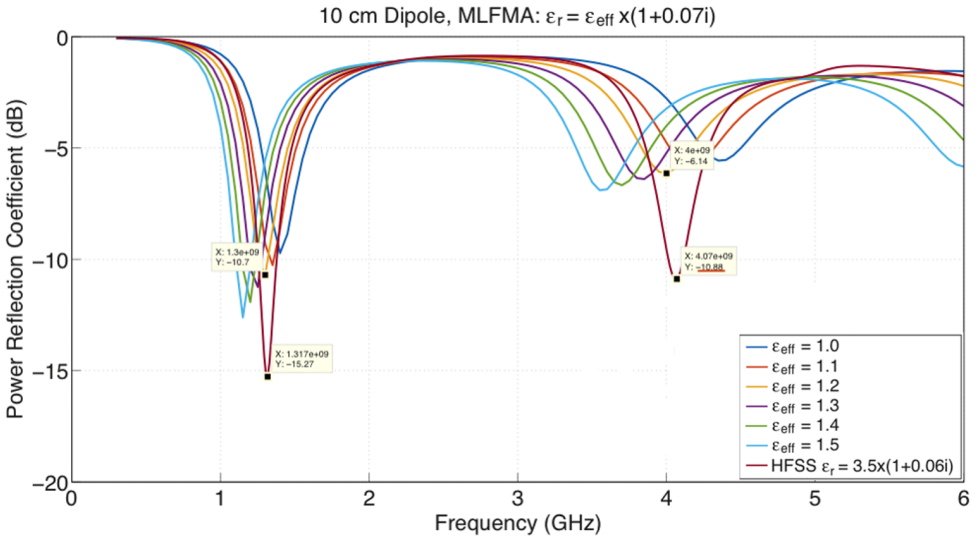

(a)



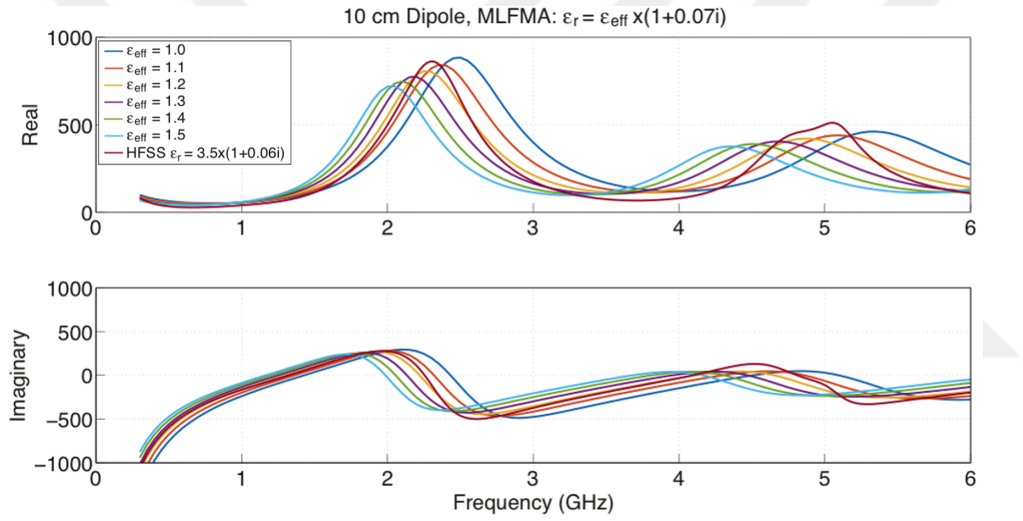

(b)

Figure 3.9: Simulation results for the 10 cm dipole antenna using HFSS with paper permittivity $3.5\times(1+i0.06)$ vs MLFMA with $\epsilon_{eff}\times(1+i0.06)$ everywhere; (a) reflection coefficient (b) input impedance

of the surrounding medium is set in MOM/MLFMA as $\epsilon_{eff} \times (1 + itan\delta)$ where $\epsilon_{eff}$ and $tan\delta$ are parametrically changing. The most consistent results shown in Figure 3.13 and Figure 3.14 are obtained when $\epsilon_r = 1.3 \times (1 + i0.01)$, which are different in comparison to the best value for the linear dipole.




(a)

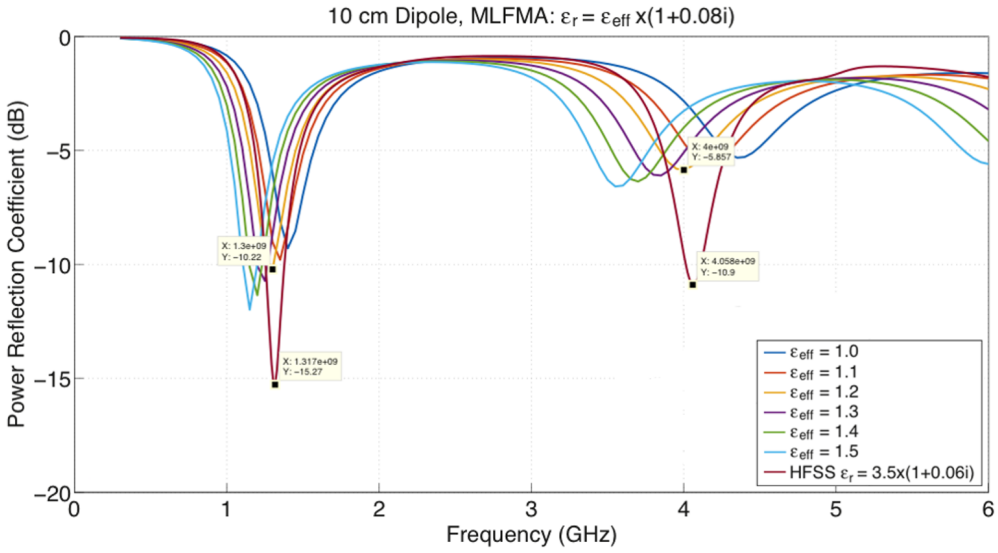



(b)

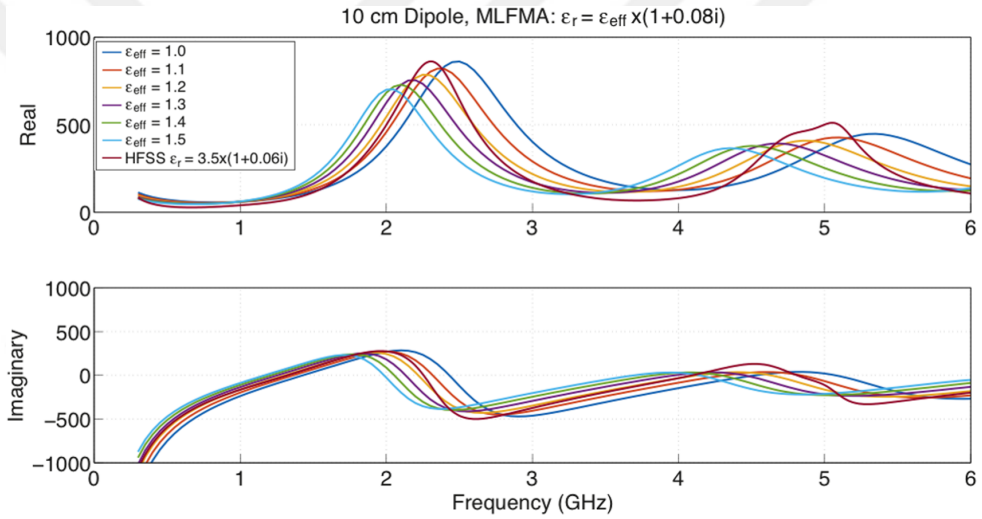
Figure 3.10: Simulation results for the 10 cm dipole antenna using HFSS with paper permittivity $3.5\times(1+i0.06)$ vs MLFMA with $\epsilon_{eff}\times(1+i0.07)$ everywhere; (a) reflection coefficient (b) input impedance

## 3.4 Impedance Matching for RFID Antennas

The antennas that are designed for RFID applications have complex input impedances on the contrary to traditional 50 Ω or 75 Ω antennas. Obviously, most of the power must be transmitted to the chip for maximum tag perfor-



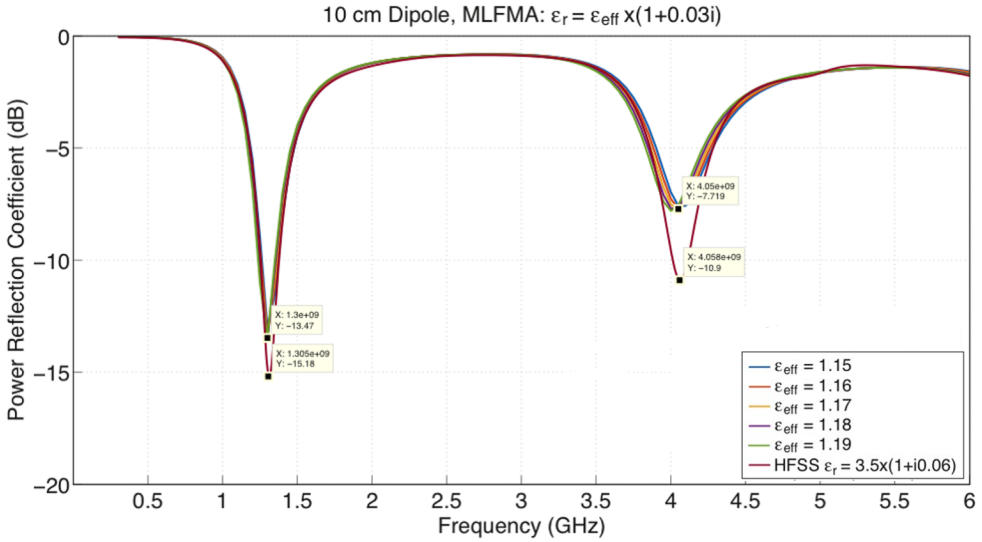

(a)



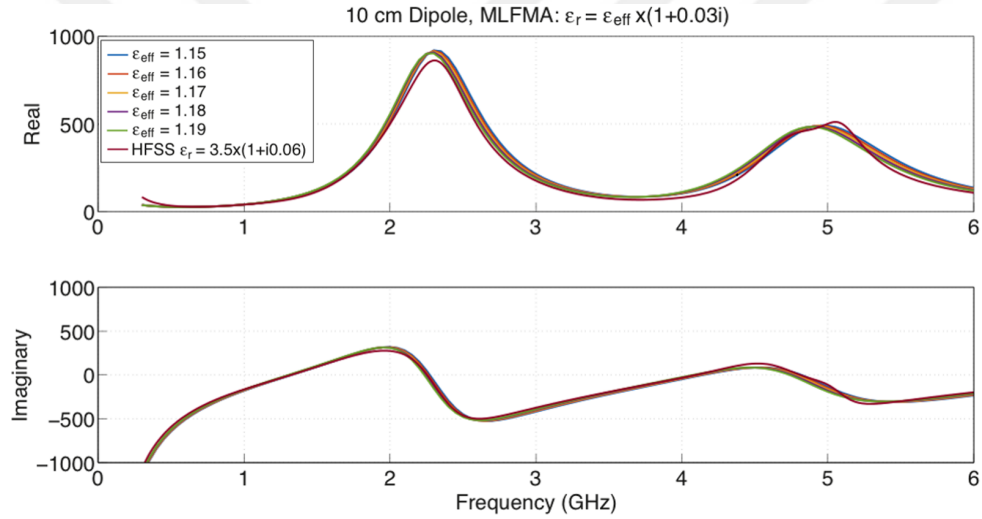

(b)

Figure 3.11: Simulation results for the 10 cm dipole antenna using HFSS with paper permittivity $3.5\times(1+i0.06)$ vs MLFMA with $\epsilon_{eff}\times(1+i0.08)$ everywhere; (a) reflection coefficient (b) input impedance

mance [21]. For the maximum power transfer, the antenna and chip need to be conjugately matched. As shown in Figure 3.15, the overall structure can be modeled as a complex source impedance for the tag antenna and as a complex load impedance for the microchip, where $Z_A$ is the tag antenna input impedance. The impedance of the load $Z_L$ is 20.55-i191.2, which corresponds to the impedance




(a)




(b)

Figure 3.12: Simulation results for the 10 cm dipole antenna using HFSS with paper permittivity $3.5\times(1+i0.06)$ vs MLFMA with $\epsilon_{eff}\times(1+i0.03)$ everywhere; (a) reflection coefficient (b) input impedance

of the used chip in this study at around 865 MHz.

Kurokawa proposes a method for the situation that connecting a complex impedance directly to another complex impedance without a transmission line between them [26]. The power reflection coefficient shows the power that cannot be transmitted to the load from maximum power of the generator and defines

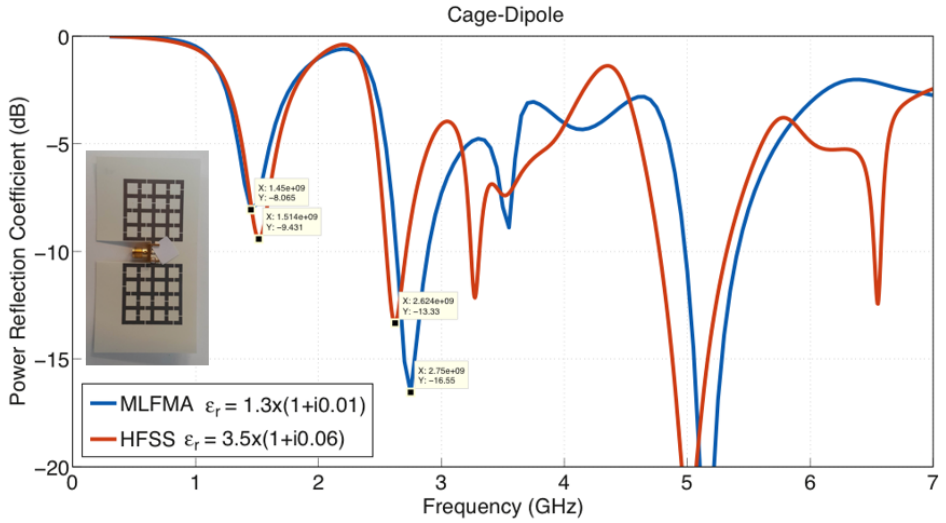



Figure 3.13: Simulation results of reflection coefficient for a cage-dipole antenna using HFSS with paper permittivity $3.5 \times (1 + i0.06)$ vs MLFMA with $1.3 \times (1 + i0.01)$ everywhere

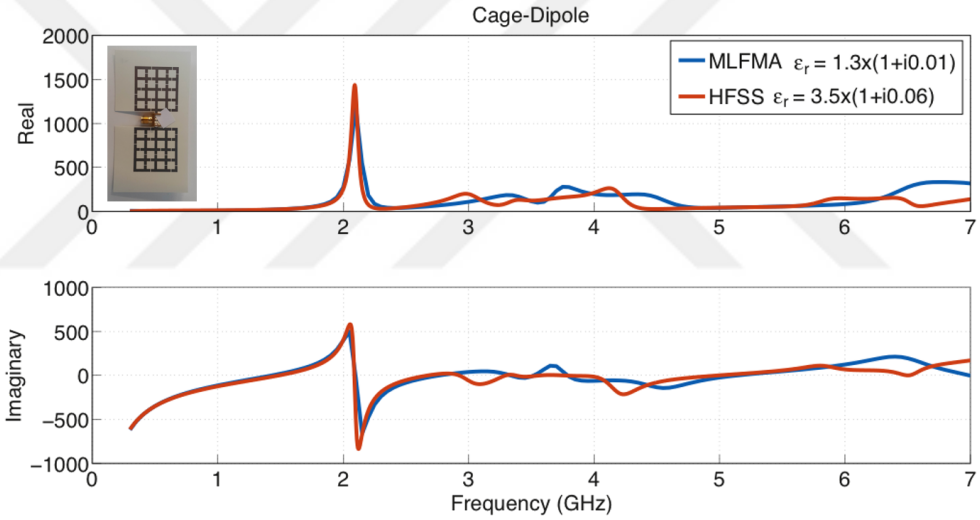



Figure 3.14: Simulation results of input impedance for a cage-dipole antenna using HFSS with paper permittivity $3.5 \times (1 + i0.06)$ vs MLFMA with $1.3 \times (1 + i0.01)$ everywhere

the tag performance and reading range of the antenna. Kurokawa describes the power reflection coefficient graphically plotting it on the Smith chart with the relation of scattering matrix. The constant power circles are located at the origin of the chart which is defined as a conjugate match ($Z_L = Z_A^*$). This method explains the maximum power transfer to the load with the power waves and power reflection coefficient when the load and generator impedances are

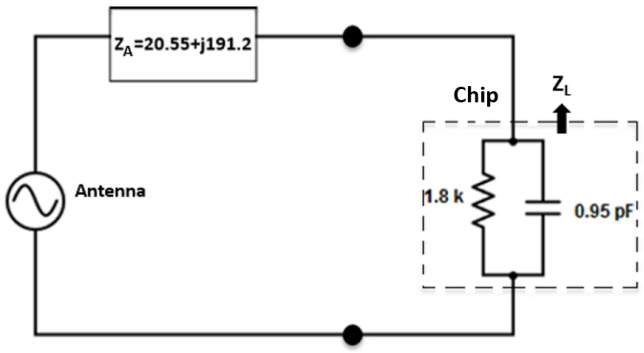



Figure 3.15: Circuit model of a passive RFID tag with complex antenna and chip impedances

imaginary. It is different from traditional voltage reflection coefficient where the load impedance is accepted purely real impedance. The power wave reflection coefficient $s$ and the power reflection coefficient $|s|^2$ are defined as

$$s = \frac{Z_L - Z_A^*}{Z_L + Z_A}$$

$$|s|^2 = |\frac{Z_L - Z_A^*}{Z_L + Z_A}|^2,$$

respectively, where $Z_L$ is the complex chip impedance and $Z_A$ is the input impedance of the antenna [26]. For minimizing s, the impedance of the antenna should be around $20.55 + i191.2$, which is highly inductive. Antenna input impedance and microchip impedance are complex in a passive RFID tag. This is completely coherent to definition of power reflection coefficient and this method can be applied to RFID applications. The power reflection coefficient analysis for a passive RFID tag is given in [27]. This is a very important challenge for RFID tags, if the antennas must be fabricated via low-cost inkjet printing. Specifically, since we are unable to print a matching network on the paper, we must find antennas that have naturally inductive input impedances. The next chapter presents solutions to this challenge, as the major work of this thesis.

# CHAPTER 4

# MAIN RESULTS AND DISCUSSIONS

## 4.1 Introduction

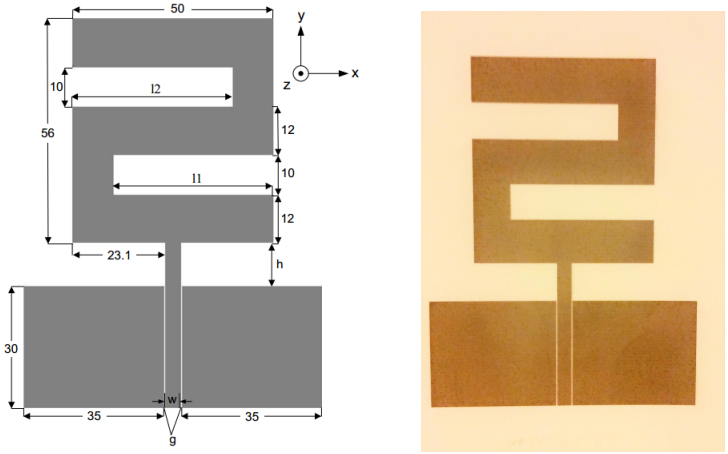
The summary of the literature about methods and design procedures of inkjet-printed antennas are presented in previous chapters. In this chapter, results and discussions for the designed and printed antennas are presented. Design stages of the antennas are explained in detail, in addition to simulation and measurement results.

## 4.2 Design, Simulation and Measurement of S-Monopole Antennas

### 4.2.1 Stages of the Antenna Design

As an initial work, S-monopole coplanar waveguide-fed (CPW) antenna, proposed in [2], is implemented on photo paper substrate. The geometry of the proposed antenna is given in Figure 4.1 (a) where l1 = l2 = 40 mm and the printed antenna in this work is given in Figure 4.1 (b) in mm. The entire size of the antenna is 74 mm (width) × 94 mm (length) including the feeding line. The antenna consists of two meander rectangular slits with widths of 10 mm and lengths of 40 mm. Canon inkjet photo paper is used as a substrate with the thickness of 0.254 mm. The S-shaped part of the antenna has 56 mm length and 50 mm width. The whole antenna including ground on two sides is on the same plane, making it suitable for inkjet printing. As the ground plane dimensions increase, the directivity of the antenna increases as well, because the ground

planes behave as radiating components of this antenna.




(a) (b)

Figure 4.1: S-monopole antenna (a) details of the original S-monopole design [2] (b) fabricated antenna using inkjet printing

The proposed antenna is first designed to match 50 Ω input impedance. Then, it is directly used for the RFID chip. Impedance matching is improved by changing the lengths and widths of the antenna. Conjugate impedance matching between the antenna and chip is maximized by adjusting these distances. It is observed that, especially the distance between the antenna lower edge and the ground plane influences the matching.

### 4.2.2 Simulation and Measurement Results

As discussed before, the designed antenna is modeled in Siemens NX and simulated via MLFMA. Simulation results of voltage standing wave ratio (VSWR), input impedance, and power reflection coefficient of the S-monopole antenna with respect to 50 Ω are presented in Figure 4.2. As seen from the graphs, the antenna resonates at 1660 MHz (without dielectric effects) with a reflection coefficient of -12.41 dB and VSWR ratio of 1.63.

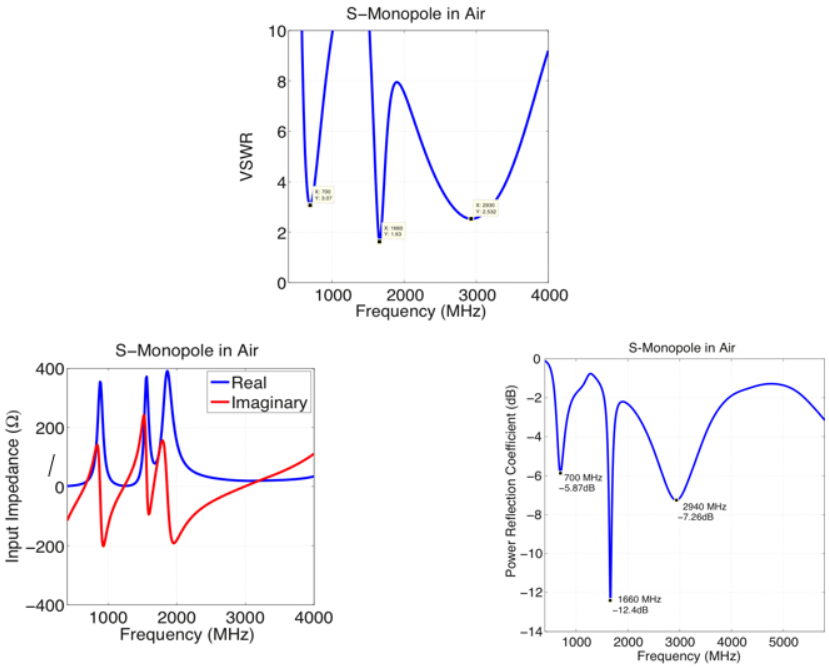



Figure 4.2: Simulation results for the S-monopole antenna

The proposed antenna is printed via a standard printer directly on a photo paper substrate using conductive silver ink. It is cured in a normal oven during 90 minutes at $150°C$ in order to have good conductivity. Measurement results of impedance and reflection coefficient of the printed antennas are presented in Figure 4.3. Measurements for a total of 18 different samples are taken via a vector network analyzer. As seen from the figure, most of the measurements are in good agreement with each other, demonstrating the stability. The discrepancies are mainly due to inkjet printing variations.

As a second design, S-monopole antenna is reshaped for matching to complex microchip impedance. Alien Technology Higgs-4 model is used as the microchip, which has $20.55 - i191.2\ \Omega$ impedance at 865 MHz. Circuit model of the microchip is given in Figure 4.4. Input impedance of the designed antenna must be conjugately matched to this impedance in a narrow UHF band (865 MHz-868 MHz).

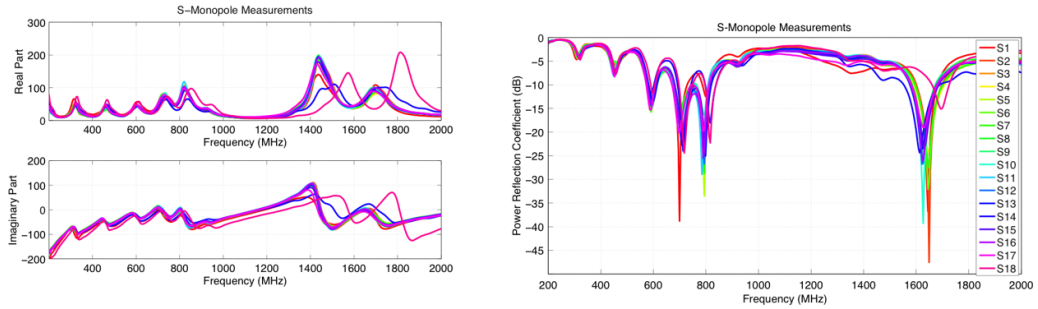



Figure 4.3: Measurement results for the S-monopole antenna when it is matched to 50 Ω

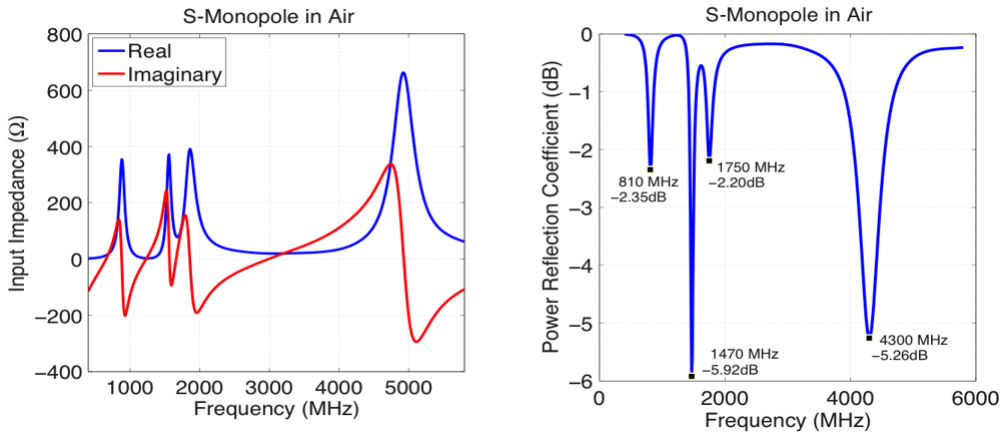



Figure 4.4: Connecting Higgs-4 IC to the designed S-monopole antenna

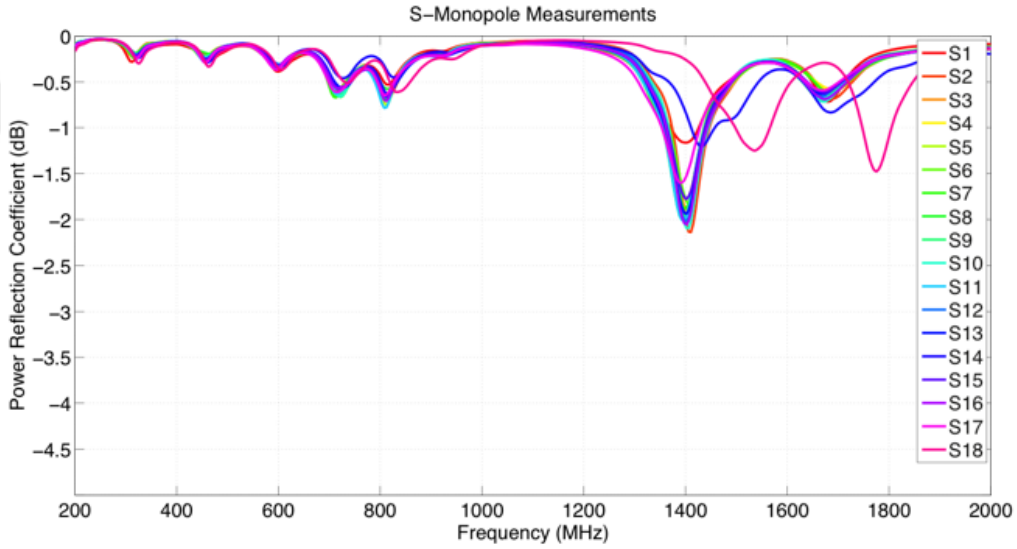
Simulation results of the S-monopole antenna that is designed for RFID is illustrated in Figure 4.5 (a). It does not have sufficient reflection coefficient values (condition of $|S_{11}| < 10$ dB) at 865 MHz. Measurement results of 18 different trials are presented in Figure 4.5 (b). These results also demonstrate the relatively poor performance of the antenna.

Since the desired results cannot be achieved, different feed points are tested, as depicted in Figure 4.6, to improve the results. Considering 50 Ω matching, feed points of 12, 13 and 14 show relatively better results, as illustrated in the reflection coefficient and current distribution graphs in Figures 4.7 and 4.8. At 1.11 GHz, the antenna support high current distribution everywhere. Measurement results for a revised antenna, which is excited at feed-13, are presented in Figure 4.9. Despite all efforts, even the modified antenna design does not match to the complex impedance, while there is no problem for matching to 50 Ω.

After numerous trials, silver conductive epoxy is used to obtain more reliable




(a)




(b)

Figure 4.5: (a) Simulation results for the RFID S-monopole antenna (b) the corresponding measurement results

measurement results. Attaching the connector using epoxy is an irreversible operation; therefore, the epoxy method is applied after measurements with physical pressure.

An overall picture of measurement results for the antennas with and without epoxy connections is given in Figure 4.10. Results are obtained as good match to 50 Ω but poor match to the microchip impedance. In the figure, the blue lines symbolize the epoxy connected antennas, and these antennas generally

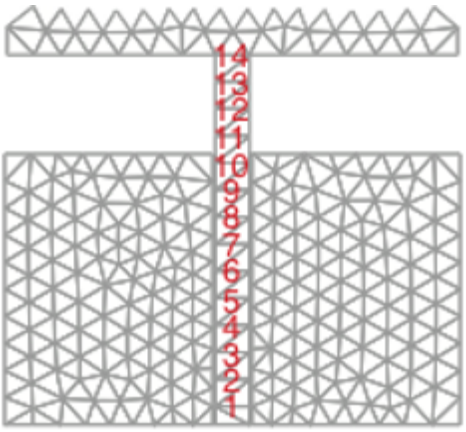



Figure 4.6: Places of feed points on the S-monopole design

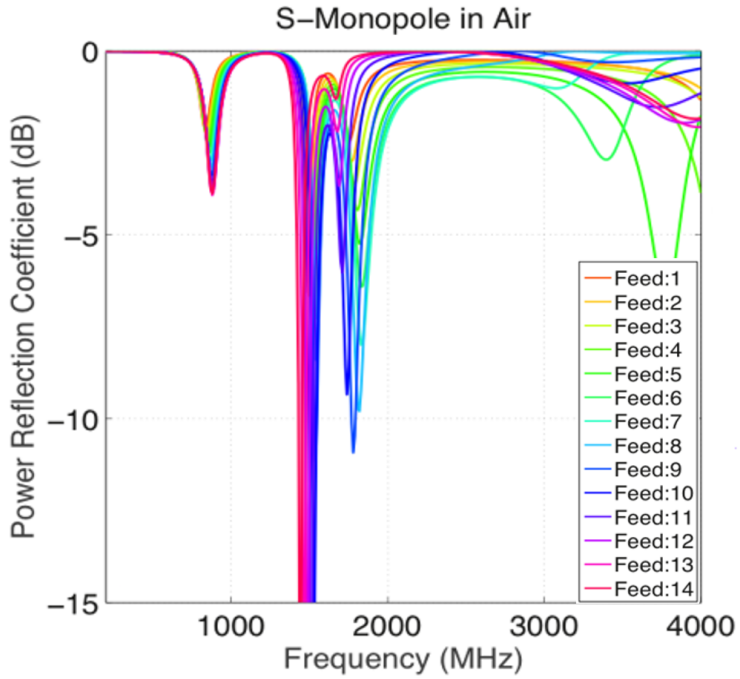



Figure 4.7: Simulation results of feed location trials for the S-monopole antenna matching to 50 Ω

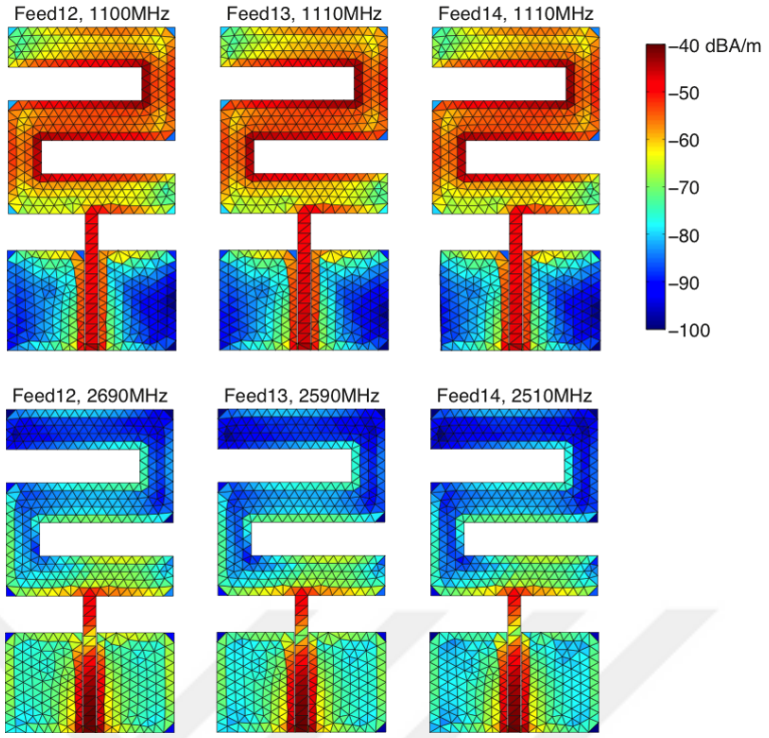



Figure 4.8: Current distributions for feeds 12, 13, and 14

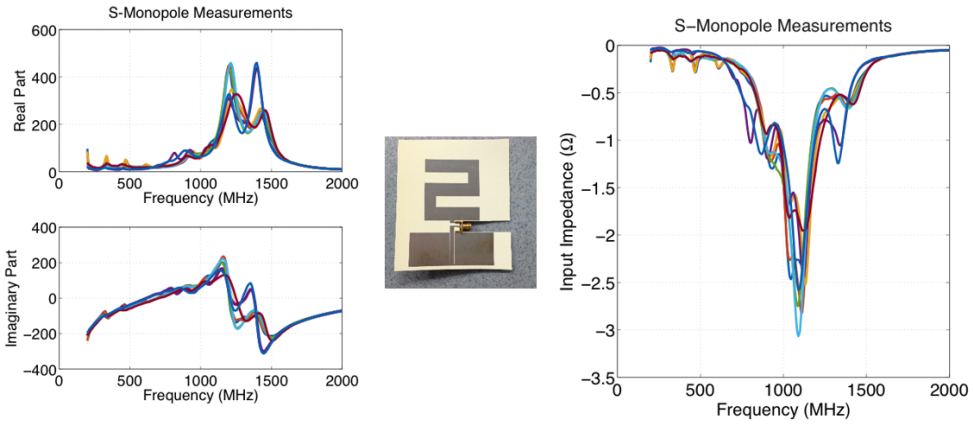
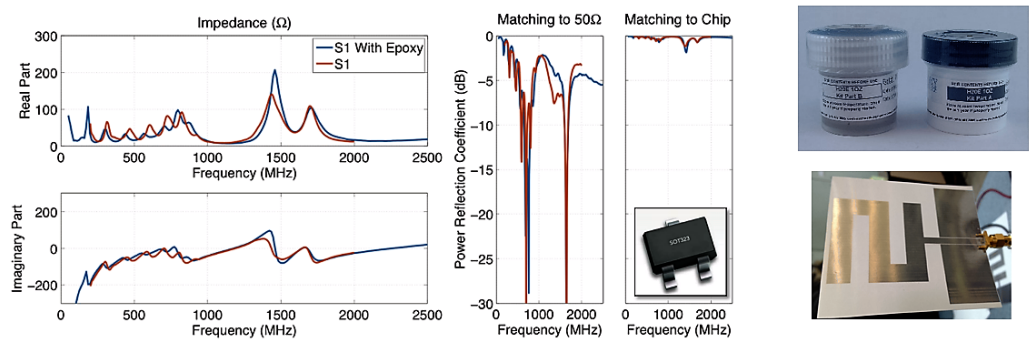



Figure 4.9: Measurement results for changed feed point

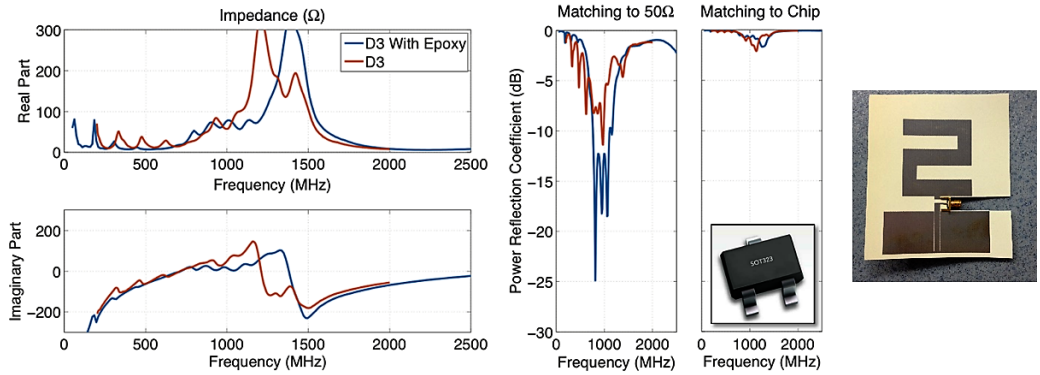
demonstrate better results, while they are still far from desired levels.

## 4.3 A Symmetric Circular Dipole Antenna

As a second type, a small symmetric dipole antenna is designed and printed onto the paper substrate. Paper is thin and has low permittivity compared to ceramic-




(a)




(b)

Figure 4.10: Measurement results for the S-monopole antenna with epoxy; (a) normal feed and (b) feed at 13th position

polymer that is used in the reference [8]. The antenna is simulated through MOM/MLFMA, the results are obtained for the air medium, and the antenna is modified to work with the desired specifications. The size of the antenna is related with the permittivity of the substrate. The antenna is designed to match to 50 Ω input impedance. The overall size of the antenna in Figure 4.11 is (5 cm x 5.3 cm). Measurement results of the reflection coefficient and input impedance are also given in the same figure. The antenna has a resonance at 867 MHz with acceptable reflection coefficient of around -15 dB. However, this antenna does not match to the chip impedance, similar to the S-monopole designs. Therefore, as discussed in the next section, we went to basics for designing new antennas suitable for RFID applications.

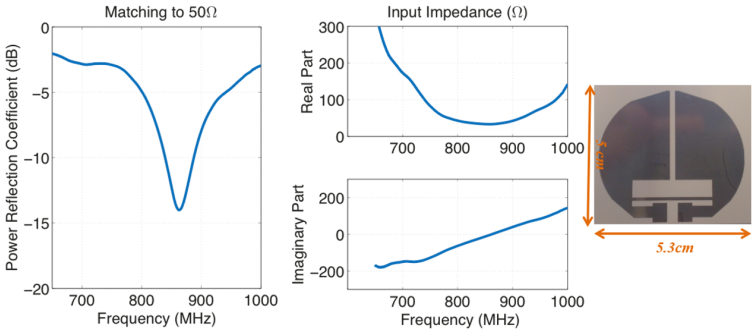



Figure 4.11: Measurement results for the symmetric circular dipole antenna when it is matched to 50 Ω

## 4.4 Design, Simulation and Measurement for Loop-Meander Antennas

### 4.4.1 Design Stages of Loop Antennas

Design of a loop antenna that is conjugately matched to the IC microchip impedance can be a preferred starting point for RFID antennas. A simple rectangular loop antenna is proposed that can match to the microchip's capacitive impedance of $20.55 - i191.2\ \Omega$ at 865 MHz. The geometry of the loop antenna is depicted in Figure 4.12; the overall size of the antenna is 13 mm (width) × 6 mm (length) in a rectangular shape. The width of conductive paths of the antenna is selected as 1.2 mm. Matching between the antenna's input impedance and the chip impedance is facilitated by tuning the antenna's length.

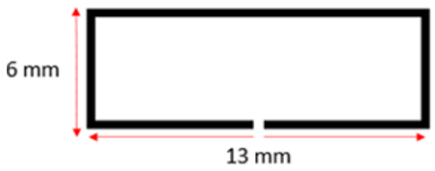



Figure 4.12: Loop antenna that is matched to chip impedance

Different types of loop antennas are also tested to gain better performance and to achieve wider bandwidth. Widths and shapes of the antennas are modified,

therefore, working frequencies, as well as characteristics of reflection coefficient and impedance values change. Reflection coefficient and input impedance values of different loops are measured via Agilent E5071C vector network analyzer, which is calibrated using 85052D calibration kit.

Some isolated loop antennas are given in Figure 4.13 with measurement results of power reflection coefficients and resonance frequencies.

| | a | b | c | d | e |
|---|---|---|---|---|---|
| Size | 13.0 mm | 13.0 mm | 14.0 mm | 12.5 mm | 14.0 mm |
| Dip Frequency | 796.3 MHz | 796.3 MHz | 995.3 MHz | 895.8 MHz | 883.3 MHz |
| Dip RC | -10.27dB | -9.795dB | -8.224dB | -12.96 dB | -11.18 dB |

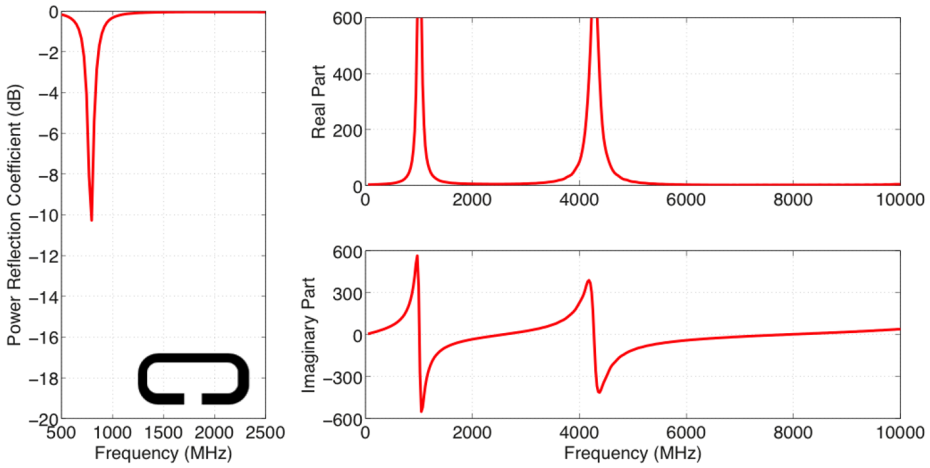
| | f | g | h | i | j |
|---|---|---|---|---|---|
| Size | 14.0 mm | 13.5 mm | 13.5 mm | 16.0 mm | 14.0 mm |
| Dip Frequency | 771.4 MHz | 1120 MHz | 1089 MHz | 721.6 MHz | 1207 MHz |
| Dip RC | -11.15 dB | -12.48 dB | -12.86 dB | -9.844 dB | -15.65 dB |

Figure 4.13: Measurement results of reflection coefficient and impedance of different loop antennas

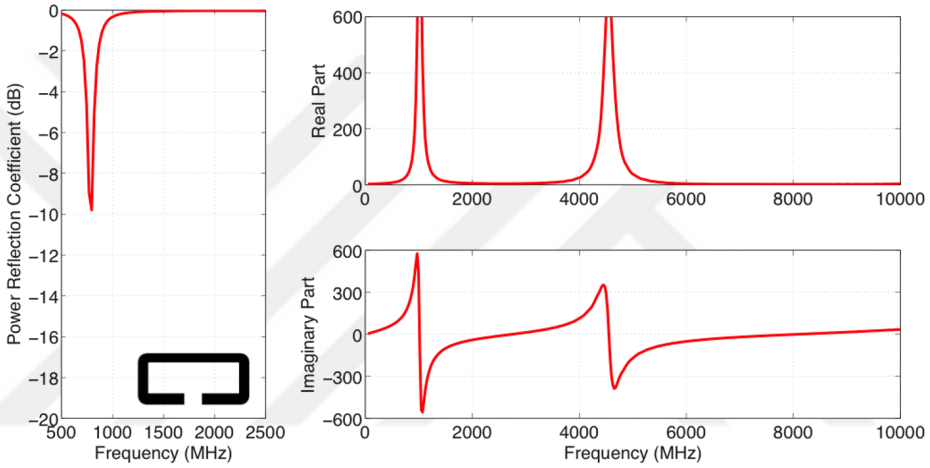
Measurement results of reflection coefficient and impedance values for different loop antennas are also shown in Figures 4.14, 4.15, 4.16, 4.17, 4.18.

Another class of isolated loop trials that are matched to microchip impedance is given in Figure 4.19, with resonance frequency and reflection coefficient results. For these antennas, detailed measurement results can be seen in Figures 4.20, 4.21, 4.22, and 4.23, respectively.

After investigating various loop designs, a meander structure with 6 turns is attached to the loop antenna to improve the reading range. For this purpose, after the evaluation of the loop trials, 13 mm (width) $\times$ 6 mm (height) rectangular loop is chosen. This type of loop is compatible with meander parts, leading to good coupling. Effect of parasitic meander part to the power-reflection coefficient values is shown in Figure 4.24 for different cases. Measurement results




(a)

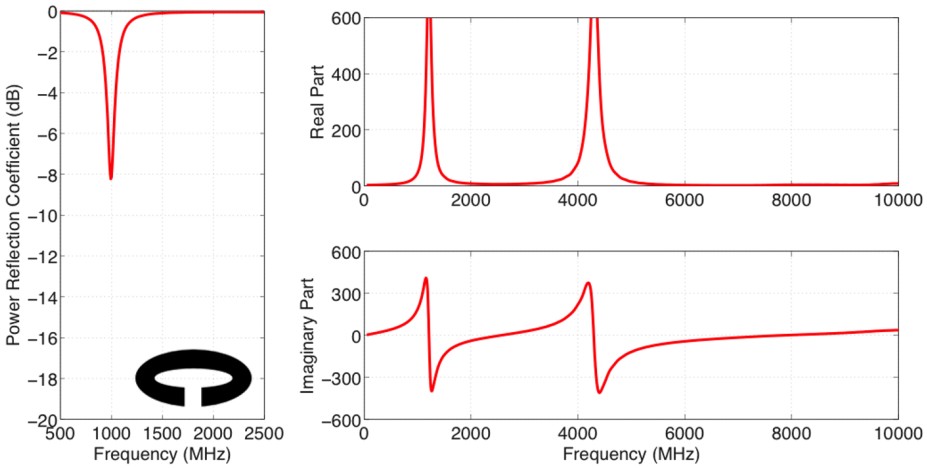



(b)

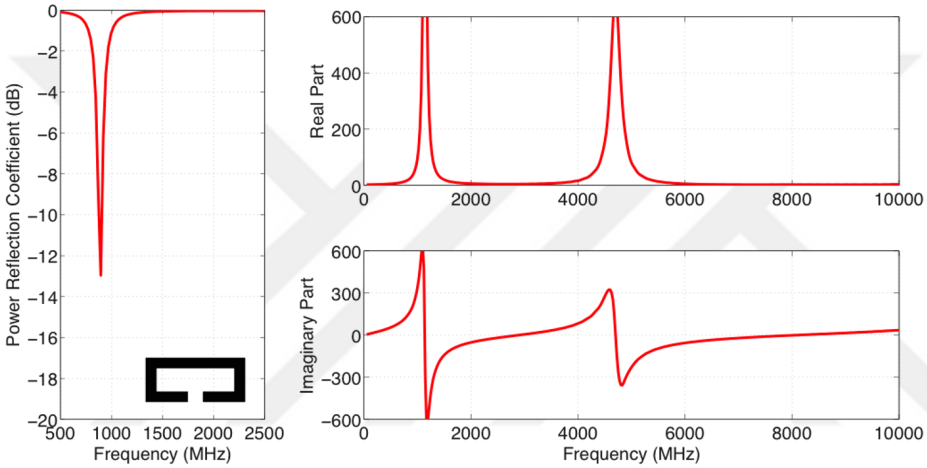
Figure 4.14: Reflection and measurement results of different loop trials; (a) loop-a (b) loop-b

are conducted via network analyzer using physical pressure method. In these experiments, the aim is to avoid changing the input impedance characteristics of the loop.

Other experiments involving epoxy connections and reversely placed parasitic meander, as well as on the loop size, are demonstrated in Figure 4.25. As expected, resonance frequency changes inversely proportional to the loop sizes. This gives us the ability to re-adjust the resonance frequency after the meander part is added.




(a)

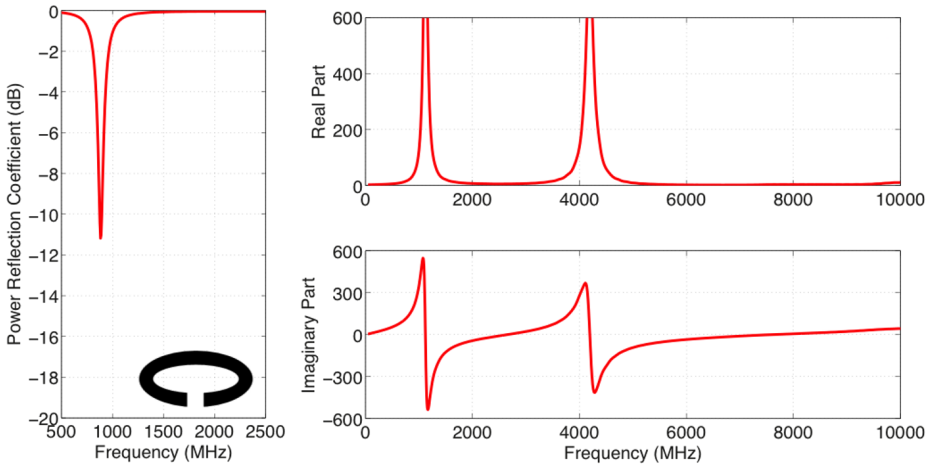



(b)

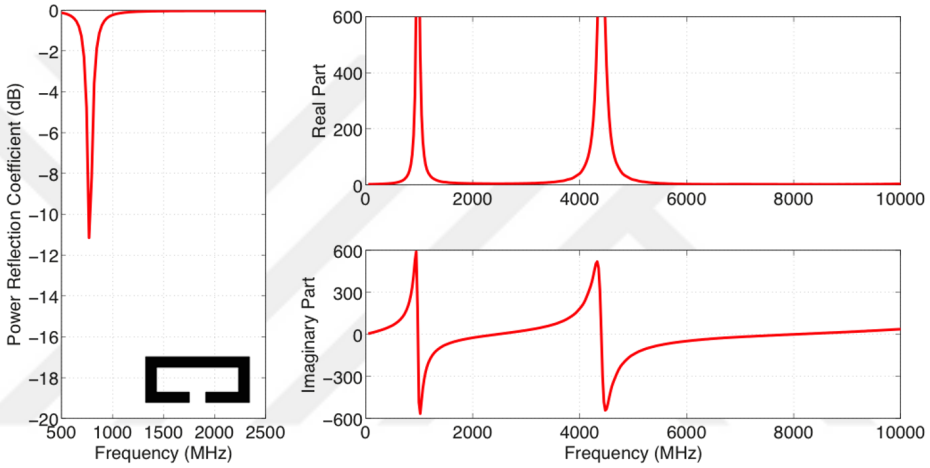
Figure 4.15: Reflection and measurement results of different loop trials; (a) loop-c (b) loop-d

### 4.4.2 Measurement Results for Loop-Meander Antennas

After many trials, the loop-meander combination is printed as a single antenna. Once again, multiple trials are performed. Measurement results are given in Figure 4.26. As it can be seen from the figures, the antenna samples have good reflection values and are conjugately matched to chip impedance at around 865 MHz. Measurement results that are obtained with physical pressure and with epoxy connections are compared in Figure 4.27.




(a)



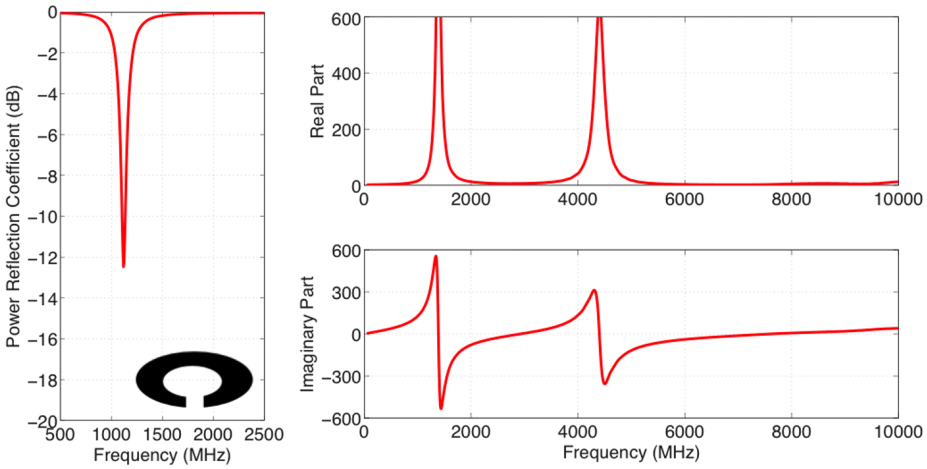

(b)

Figure 4.16: Reflection and measurement results of different loop trials; (a) loop-e (b) loop-f

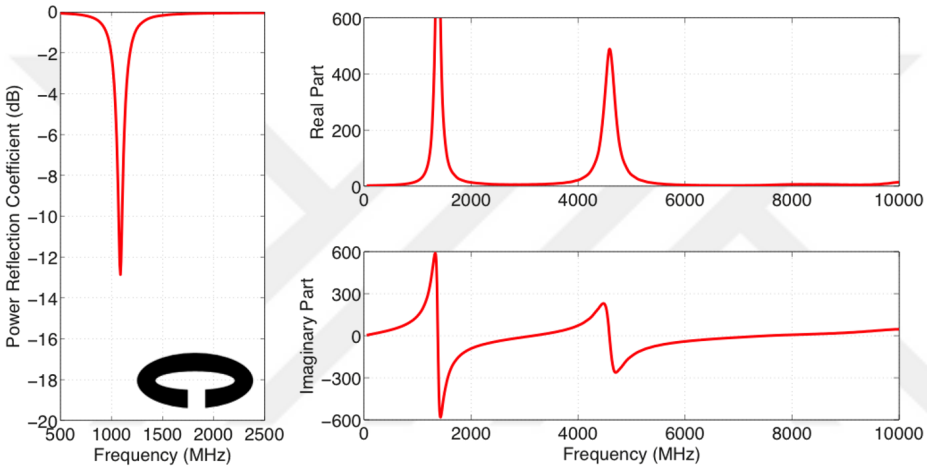
Multiple measurement results using epoxy for connections, as well as mean values are further presented in Figures 4.29, 4.28, and 4.30.

### 4.4.3 Reading Range Tests for Loop-Meander Antennas

Reading range is an important criteria for RFID antennas. As discussed above, a loop antenna is designed as conjugately matched to the chip impedance. Then, meander part is added to the loop to increase the antenna gain, hence to increase



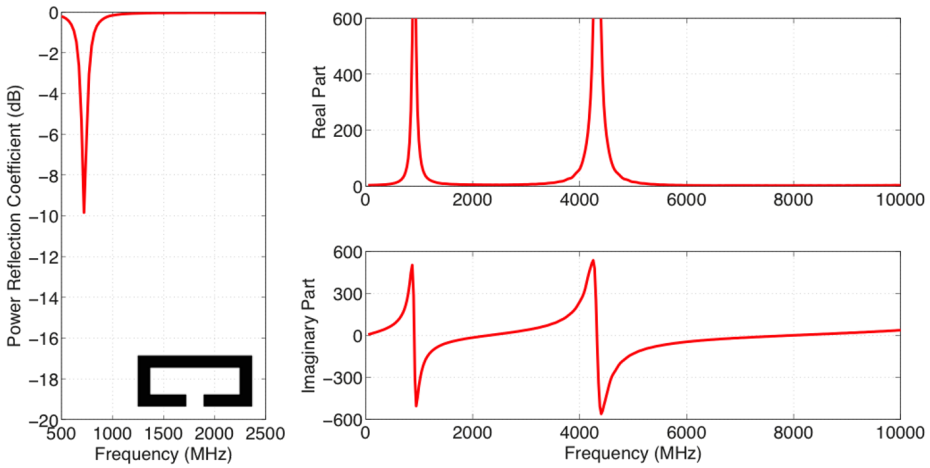

(a)



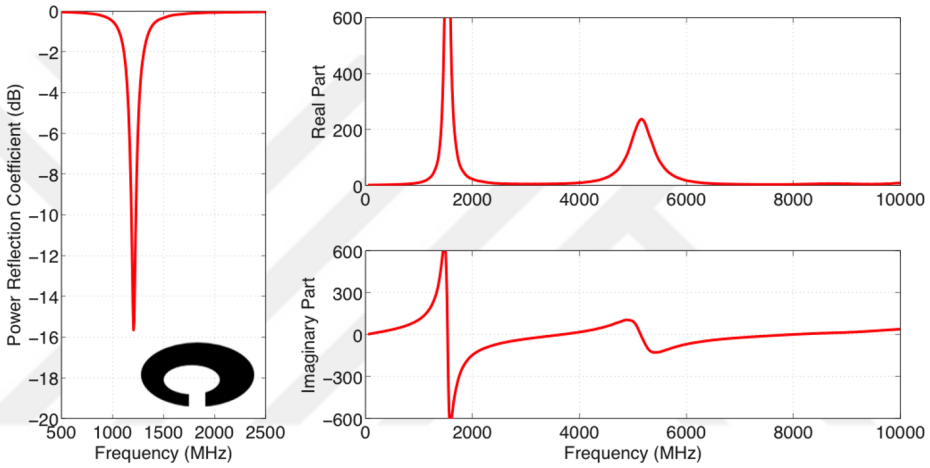

(b)

Figure 4.17: Reflection and measurement results of different loop trials; (a) loop-g (b) loop-h

the reading range of the antenna. While reading range of an isolated loop with chip is nearly 2-3 cm, it increases up to 55-60 cm after attaching the meander part as a parasitic element. We also observe that the number of turns in the meander part can change the read range characteristic of the antenna. Along this direction, meander with 5, 6, 8, 10 and 12 turns are designed and measured after attaching to the loops. Measurement results of the antennas with different number of turns (with epoxy connection) are given in Figure 4.31. According to these results, the loop with 6-turn meander has better reflection coefficient




(a)




(b)

Figure 4.18: Reflection and measurement results of different loop trials; (a) loop-i (b) loop-j

and has more stable input impedance. Therefore, 6-turn meander is chosen for further reading range tests.

Reading range tests are utilized on a table using ATID AT870 Hand-Held UHF RFID reader that is working in 865-868 MHz band with output power of 1W or 30 dBm. In reading-range tests, effect of the parasitic part are observed by using different structures, such as meanders with two different numbers of turns, a parabolic meander, and a fractal structure. In each case, the placement of the loop is optimized by considering different locations. A summary of results can be

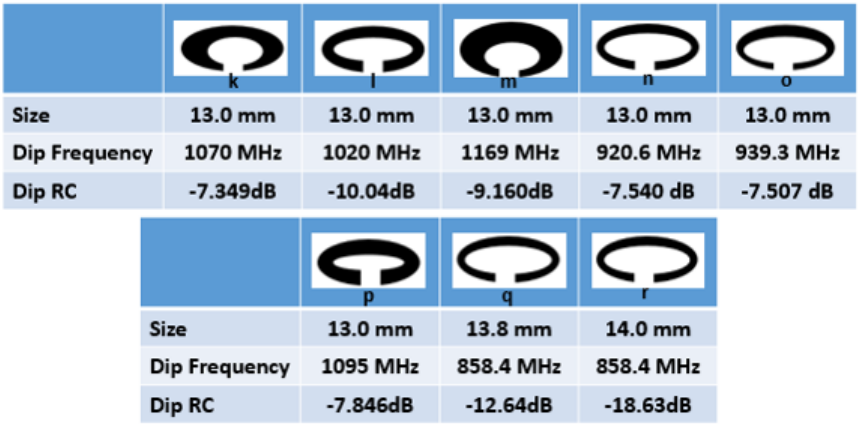


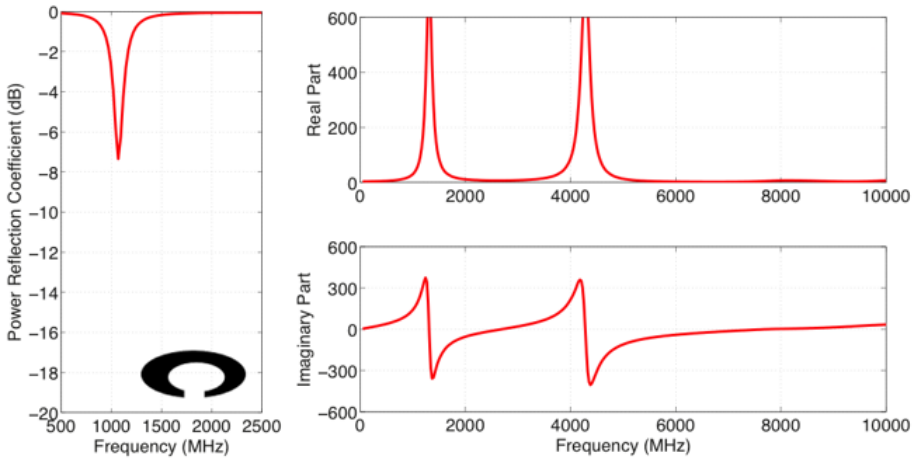

Figure 4.19: Measured reflection coefficient and impedance of loop antennas

seen in Figure 4.32. Maximum read ranges (130 cm in the figure) are obtained when the loop is placed in the middle of the 6-turn meander perpendicularly.

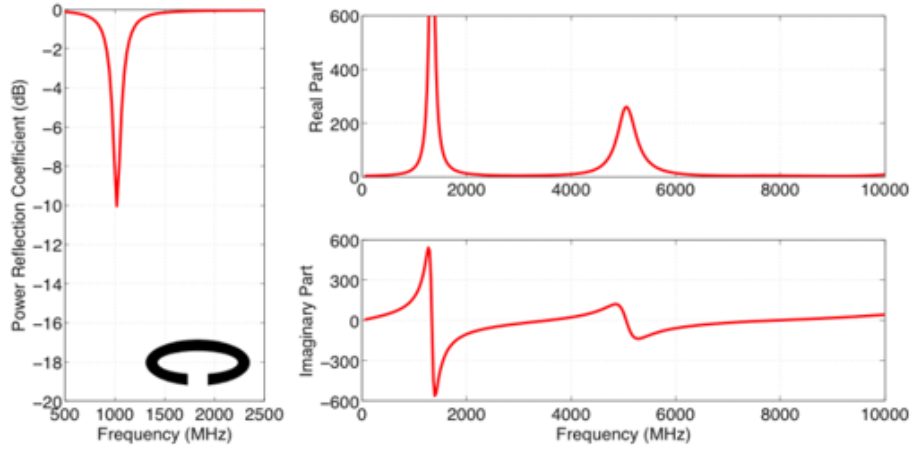
Reading range values of the 6-turn loop-meander at different angles are further tabulated in Figure 4.33 along with photographs. The antenna is located on a wooden table (with zero distance) on $x-y$ axis and rotated discretely with 30° angles from 0° to 360°. This way, we obtain 1D reading range pattern of the antenna.

Second measurement setup consists of rotatable foam parts for scanning reading range of the antenna at all angles. Antenna is located on a rotated foam that can be scanned for $\theta$ from 0° to 180° and for $\phi$ from 0° to 360° with 15° degrees. For every $\theta$ value, $x-y$ plane is scanned entirely at intervals of 15°. Measurement setup at different angles and reading ranges as a colored graph (in cm) are shown in Figure 4.34. Reading range graph shows that the antenna exhibits 60 cm as a maximum range. This antenna can be used at different RFID applications since these ranges are satisfactorily acceptable in most cases.

As a final check, a fractal structure is attached to the loop antenna as parasitic element to increase the reading range. In order to obtain maximum range, the loop antenna is positioned properly. Reading range tests are realized at different angles. Measurement setup and reading ranges as in a colored graph are given in Figure 4.35. Although the maximum reading range is nearly the same with




(a)

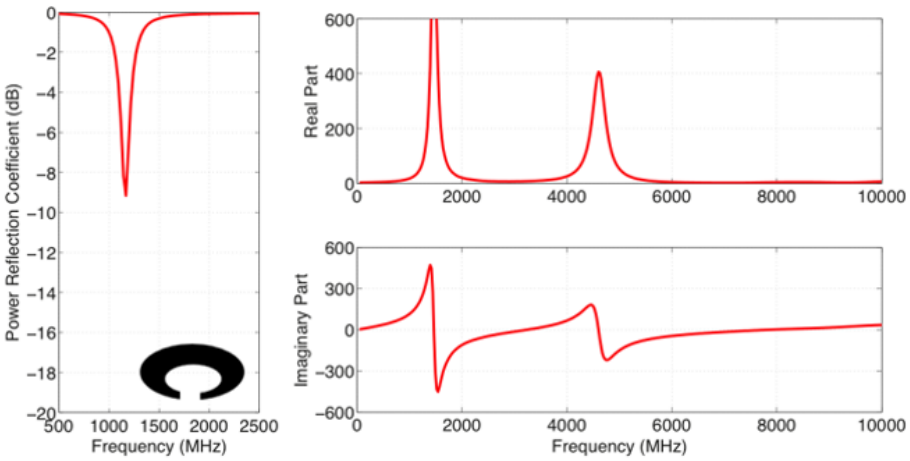



(b)

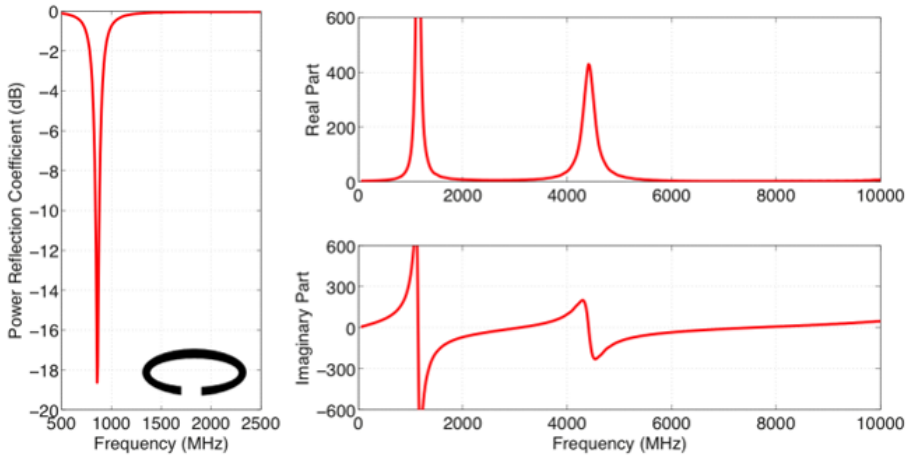
Figure 4.20: Reflection and measurement results of different loop trials; (a) loop-k (b) loop-l

the rectangular meander, there are serious dips that limit the usage of the loop-fractal combination.

Finally, the loop-meander antenna is tested on different materials, such as plastic, metal, and foam, to observe the effects of the environment. The results indicate that by increasing the foam thickness of the bottom layer, reading range decreases. Obviously, the antenna benefits from a dielectric support. When the antenna is placed onto a conductor it completely fails. These results of range values are depicted in Figure 4.36.



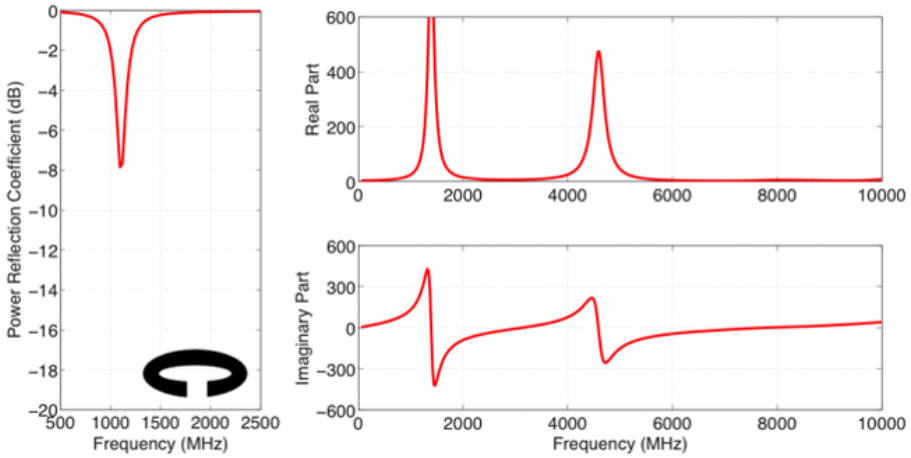

(a)



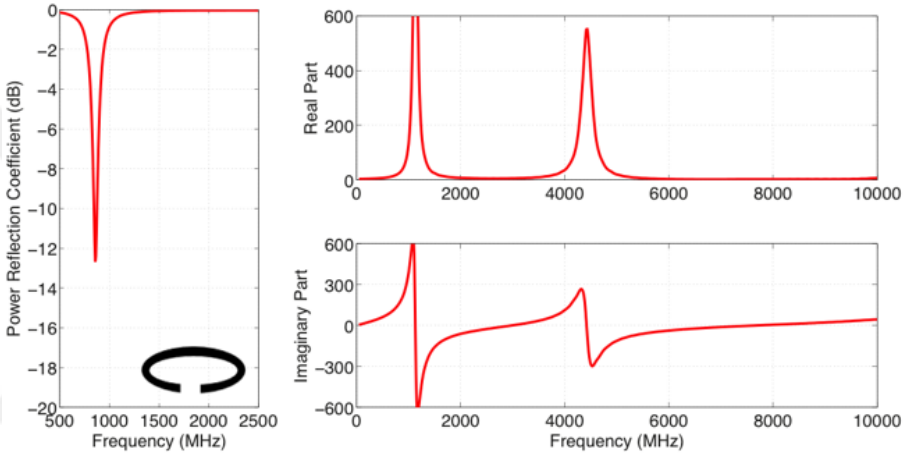

(b)

Figure 4.21: Reflection and measurement results of different loop trials; (a) loop-m (b) loop-n

Figure 4.37 reveals that the designed antennas can also be used on human body for RFID applications. The antennas with meander and fractal parts are tested at two different positions. In these experiments, the target is kept stable, while the reader is steering with 15° from 0° to 180° on the $x-y$ plane. As the figure shows the results are much better when the antenna is located at around waist.




(a)

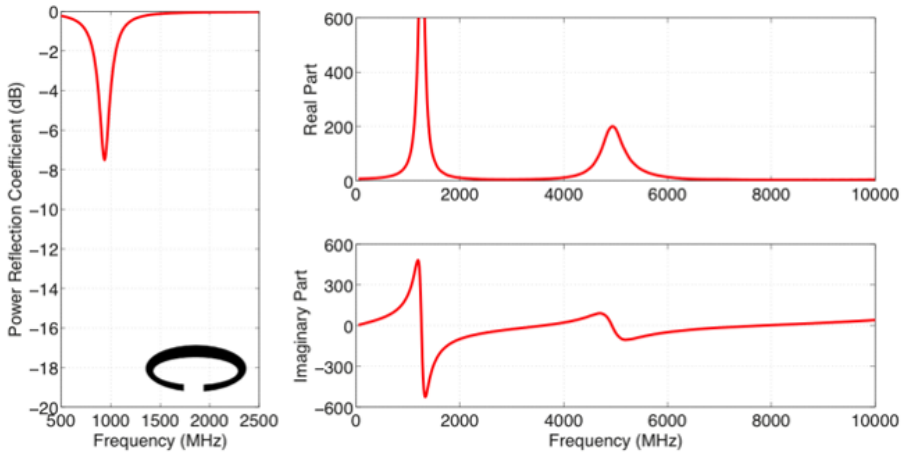



(b)

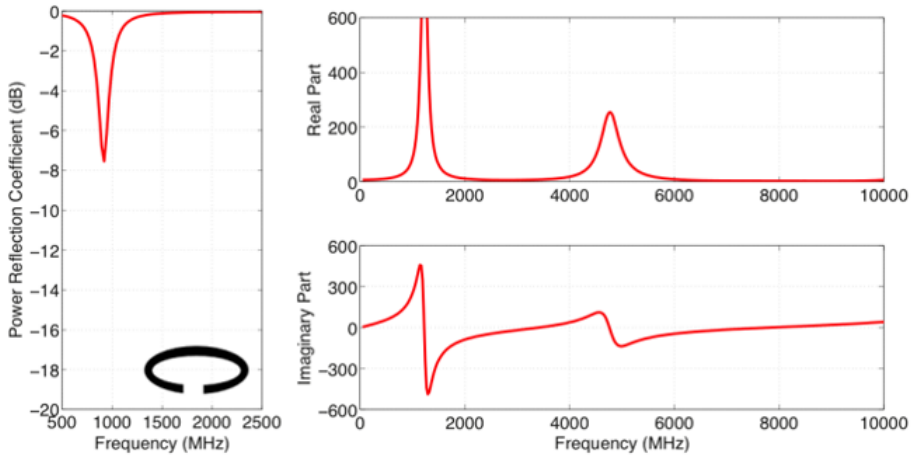
Figure 4.22: Reflection and measurement results of different loop trials; (a) loop-o (b) loop-p

## 4.5 Optimized Cage-Dipole Antennas

In this section, we present cage-dipole antennas that are optimized using an efficient optimization environment based on MLFMA and genetic algorithms. Genetic algorithms provide different antenna combinations for different radiation patterns and desired antenna characteristics. Since genetic algorithms require thousands of trials, MLFMA is used as the solver, despite relatively small sizes of the antennas [17].




(a)

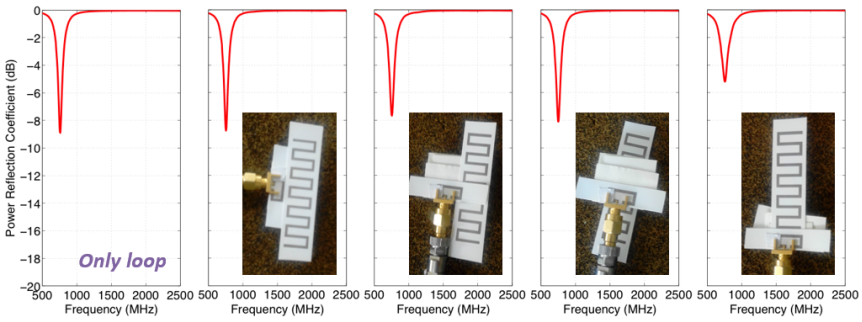



(b)

Figure 4.23: Reflection and measurement results of different loop trials; (a) loop-q (b) loop-r

### 4.5.1 Optimization Steps of Cage-Dipole Antennas

The proposed antenna structure consists of gap positions, which are opened or closed according to the results of the optimizations. Specifically, gaps operate as switches (on-off) for desired radiation characteristics, such as the directive gain. Different antenna configurations are obtained with combinations of open/closed gaps. In the optimizations presented in this thesis, the cost function is defined as $CF = (1 - |\Gamma|)D(\theta_0 = 0)$, where $D(\theta_0 = 0)$ is the directive gain in the $z$ direction when the antenna is located on the $x - y$ plane. Hence, the purpose




| 761.3 MHz | 755.3 MHz | 755.3 MHz | 755.3 MHz | 755.3 MHz |
|---|---|---|---|---|
| -8.898dB | -8.755dB | -7.669dB | -8.102 dB | -5.204 dB |

Figure 4.24: Effects of the parasitic meander part

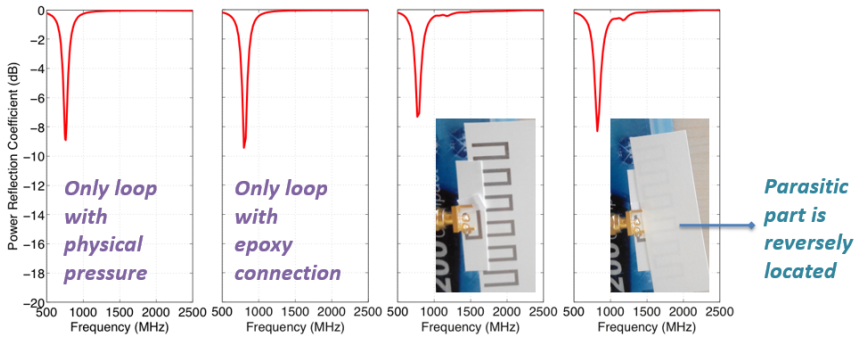
of the optimization algorithm is to maximize the directive gain of the cage-dipole antennas. We particularly focus on a type of cage-dipole antennas that consists of a total 80 gaps, therefore there are $2^{80} \approx 1.21 \times 10^{24}$ different gap configurations. Since the considered cage-dipole antenna has symmetrical gap positions according to the feed point, the number of possible configurations reduces to $2^{40} \approx 1.10 \times 10^{12}$.

After each optimization, the obtained antenna can be evaluated in two different forms involving computational gaps and modeled gaps. For computational gaps, the opened gaps are created computationally as the RWG functions of the opened gaps are assigned to zero. For modeled gaps, the optimized antenna is re-modeled via Siemens NX with real gaps of 0.5 mm to verify the performance of the antenna before the fabrication.

Design steps for the optimization of cage-dipole antennas are summarized as follows.

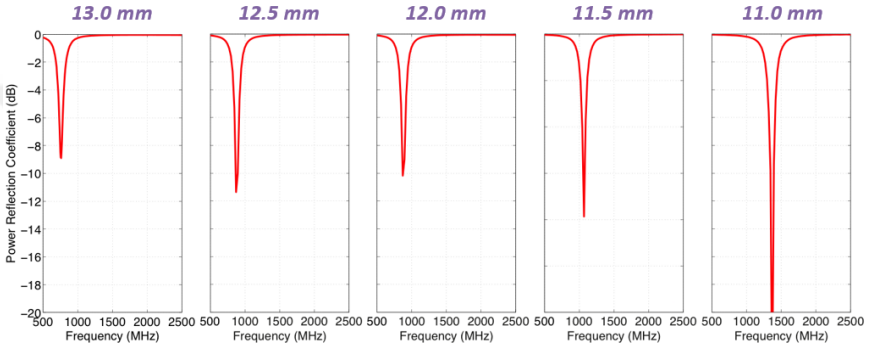
**1.** Unoptimized cage-dipole antenna is referred when the all the gaps are closed. Unoptimized structure is optimized by genetic algorithms to obtain desired antenna characteristics with given specifications. The overall size of the antenna geometry is 3.2 cm $\times$ 6.8 cm as shown in Figure 4.38 with gap locations.

**2.** Antenna is matched to the desired impedance. For 50 $\Omega$ matching, the optimization frequency is selected as 1.5 GHz. The antenna is also matched to




| 761.3 MHz | 796.3 MHz | 771.4 MHz | 821.1 MHz |
|---|---|---|---|
| -8.898dB | -9.443dB | -7.316dB | -8.303 dB |

(a)



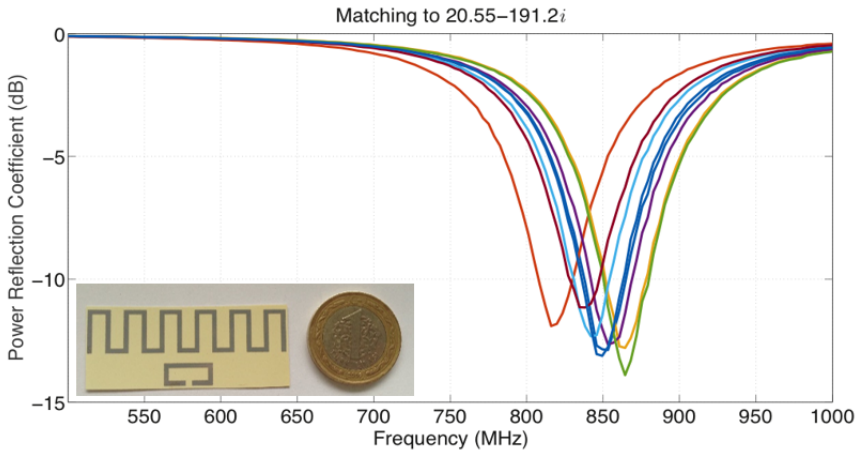

| 761.3 MHz | 870.9 MHz | 870.9 MHz | 1070 MHz | 1368 MHz |
|---|---|---|---|---|
| -8.898dB | -11.36dB | -10.18dB | -19.67dB | -26.67dB |

(b)

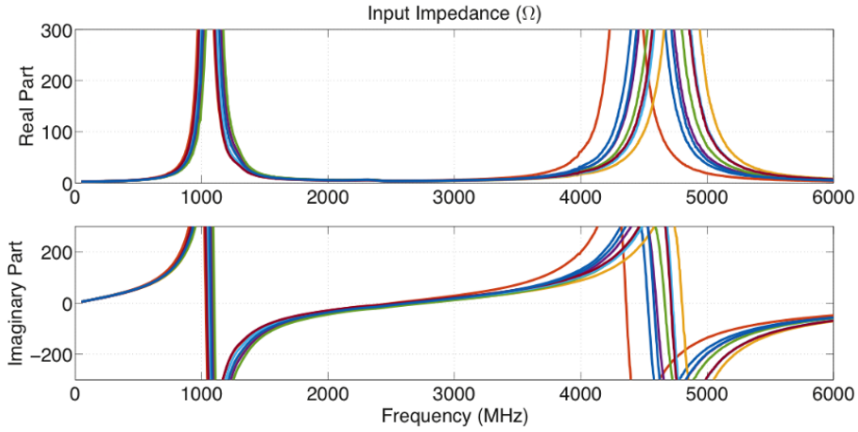
Figure 4.25: (a) Further measurements with the loop and meander antennas, (b) effect of the loop size

the chip at 865-868 MHz. Surrounding medium is modeled with an effective permittivity of $1.3 + 0.013i$ to characterize the photo paper that is used as substrate. This permittivity value is obtained through a procedure as mentioned in Chapter 3.

**3.** The optimization algorithm gives the information of opened gaps. Hence, a new geometry is obtained with these open gap positions. Reflection coefficient can be plotted using the optimized antenna using computational gaps and modeled gaps.




(a)




(b)

Figure 4.26: Measurement results for loop-meander antennas; (a) power reflection coefficient (b) input impedance

First, we consider the results of optimizations at 1.5 GHz, when the antenna is matched to 50 Ω. Cost function values, directive gain and the return loss ($20log_{10}|\Gamma|$) of optimized antennas are tabulated in Table 4.1 for three different trials. The results are given for computational and modeled gaps, respectively. Although there are differences between the results of computational and modeled gaps, the antennas demonstrate the desired radiation characteristics with good values of the directive gain.

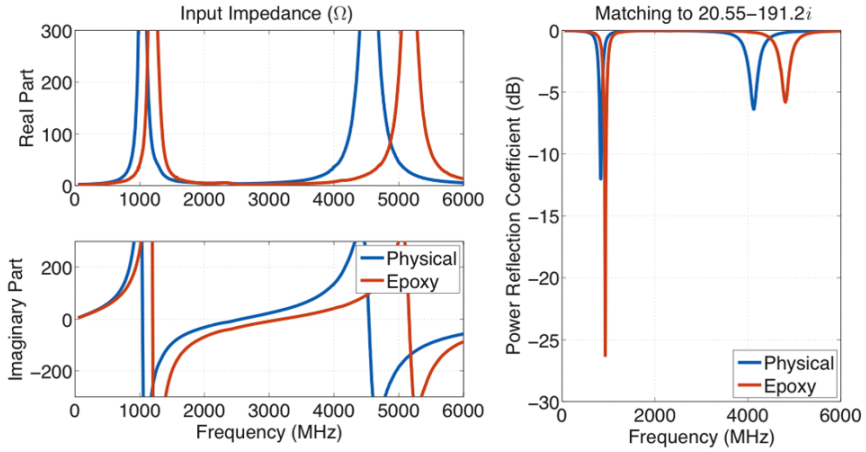



Figure 4.27: Comparison of physical pressure connection and epoxy connection for loop-meander antennas

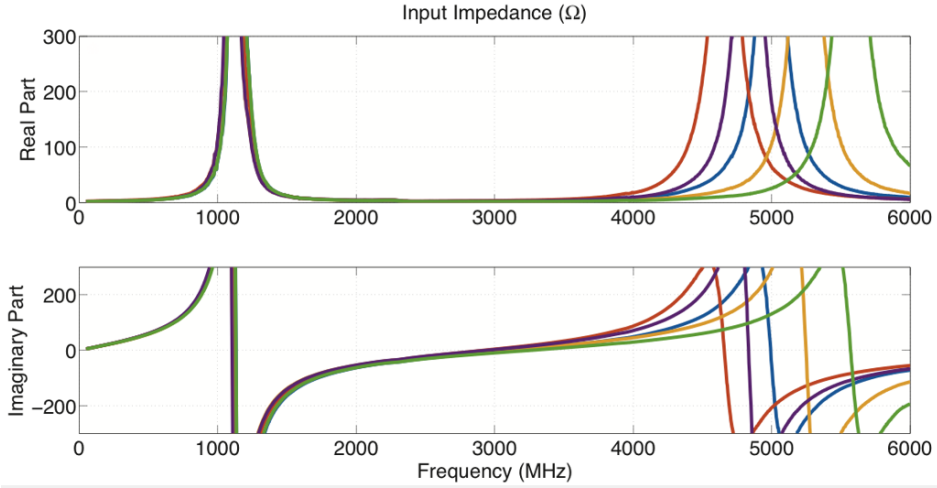



Figure 4.28: Measurement results of input impedance obtained by using epoxy to attach the connector to the loop-meander antennas

### 4.5.2 Simulation and Measurement for Cage-Dipole Antennas

The results of three different antenna optimizations are given in Table 4.1. The second trial, which has 1.8092 directive gain using modeled gaps, is chosen and further simulated. This antenna resonates at 1.5 GHz with -21.76 dB return loss, and it is also depicted in Figure 4.38, where green and red colors represent short circuit (no gap) and open circuit (gap), respectively. Current distributions at 1.5 GHz when the antenna is excited by 1V delta-gap source are shown in Figure 4.39, while the radiation patterns on the $x-z$ and $y-z$ planes with 20 dB scale can be seen in Figure 4.40 for both computational and modeled gaps.

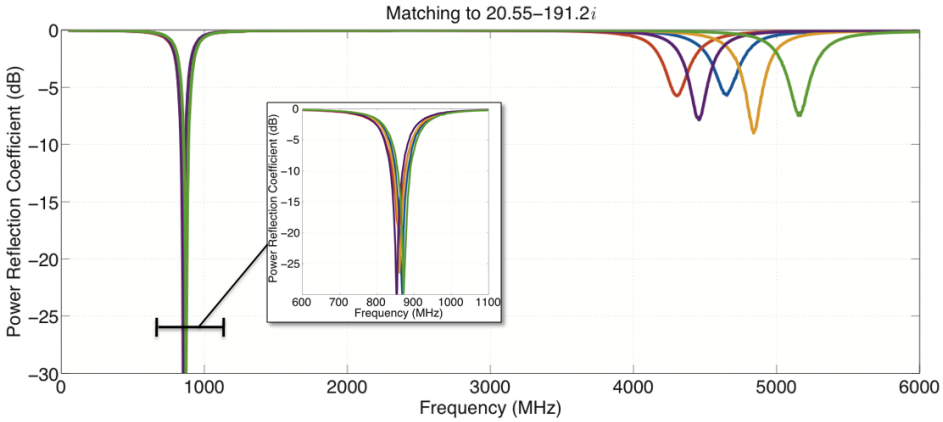



Figure 4.29: Measurement results of reflection coefficient obtained by using epoxy to attach the connector to the loop-meander antennas

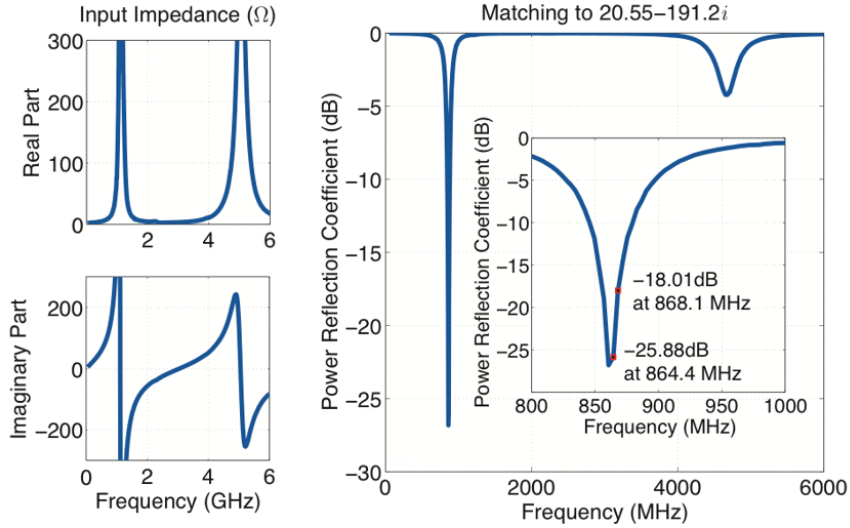



Figure 4.30: Mean measurement results for loop-meander antennas using epoxy in measurements

The radiation pattern in the $x-z$ plane presents omnidirectional characteristics, while it is the radiation pattern of a standard dipole antenna on the $y-z$ plane.

The cage-dipole antenna in Figure 4.38 is fabricated via inkjet printing. Once again, 25% alloyed silver ink is used and the antenna is cured in a standard oven at around $160°C$ for 1.5 hour. Measurement results of the reflection coefficient are obtained by using a network analyzer by connecting the SMA connector via the physical pressure method. The connection method during the measurement is shown in Figure 4.41, and the reflection coefficient results are depicted in Figure 4.42. Measurements are performed from 1 GHz to 4 GHz. A dip occurs

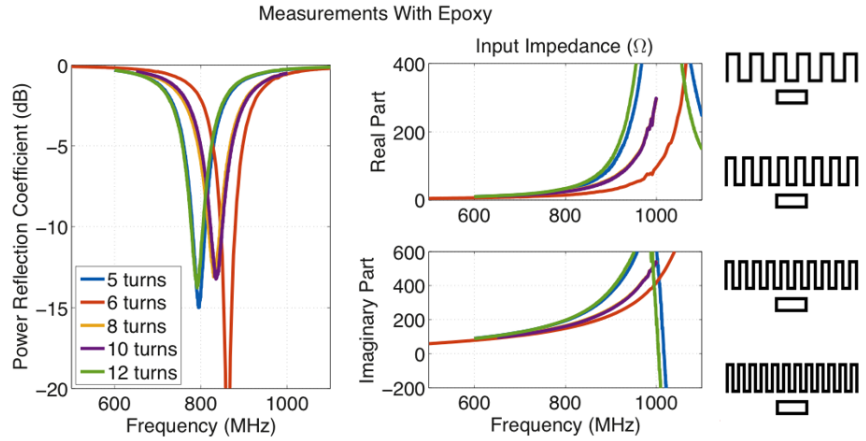



Figure 4.31: Measurement results for loop-meander antennas with different number of turns

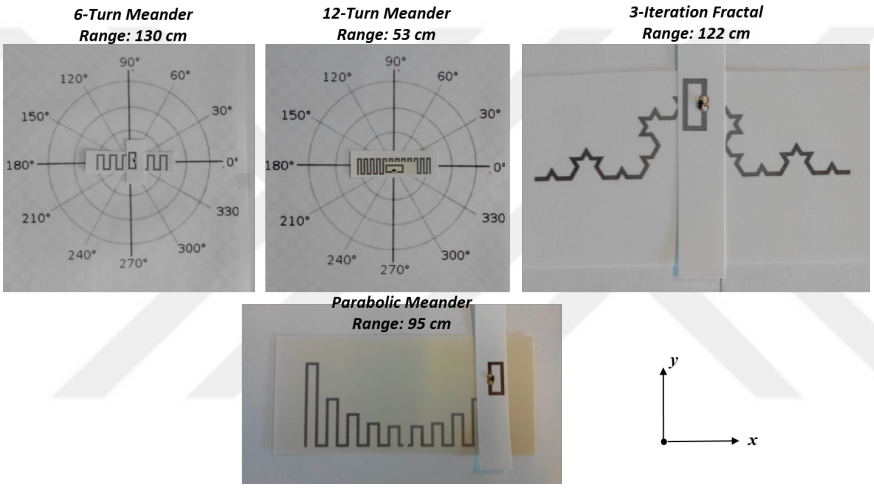
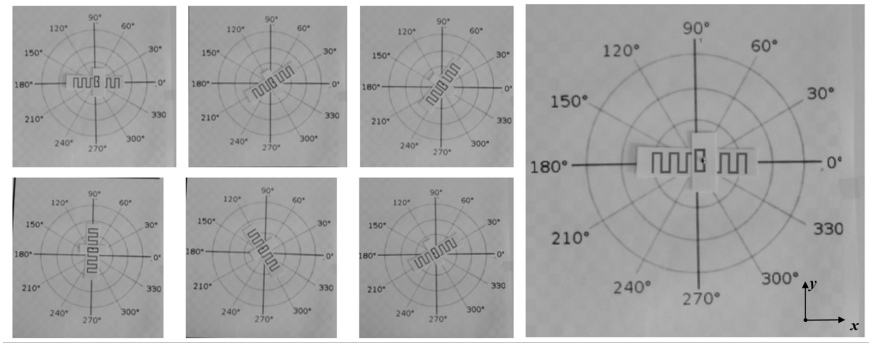



Figure 4.32: Effect of parasitic parts on the reading range

at 1.562 GHz with -23 dB reflection coefficient. Numerical results with computational and modeled gaps are consistent with a dip at 1.5 GHz. Defections in low-cost printing process and frequency dependency of permittivity cause the little frequency shift between simulation and measurement results.

## 4.6 Simulation and Reading Range Results for an Optimized RFID Cage-Dipole Antenna

Cage-dipole antennas are very convenient for RFID applications due to suitable configurations for optimizations. In this section, a cage-dipole antenna is




(a)

| Rotation | 0° | 30° | 60° | 90° | 120° | 150° | 180° | 210° | 240° | 270° | 300° | 330° |
|---|---|---|---|---|---|---|---|---|---|---|---|---|
| Range (cm) | 130 | 115 | 105 | 125 | 105 | 115 | 125 | 120 | 115 | 125 | 120 | 125 |

(b)

Figure 4.33: (a) Rotation tests for the 6-turn loop-meander antenna, (b) range values

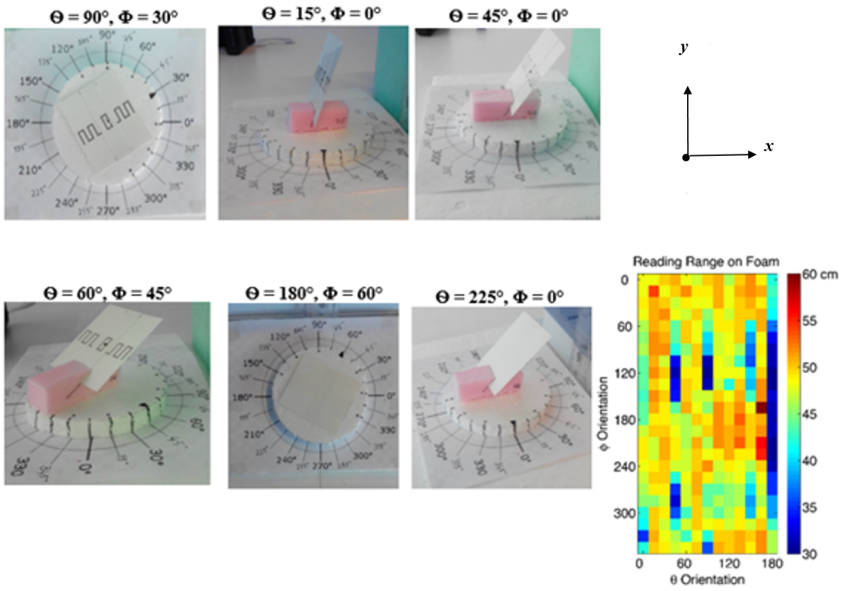



Figure 4.34: Reading tests on foam for the 6-turn loop-meander antenna

designed to match to complex microchip impedance. Similar to previous antennas, Alien Higgs-4 IC microchip is used in this design. Medium effective permittivity is modeled as $1.3 \times (1 + i0.01)$. The optimization frequency is set to 865 MHz and the purpose of the optimization is selected as the maximization of the directive antenna gain at this frequency. The overall size of the optimized

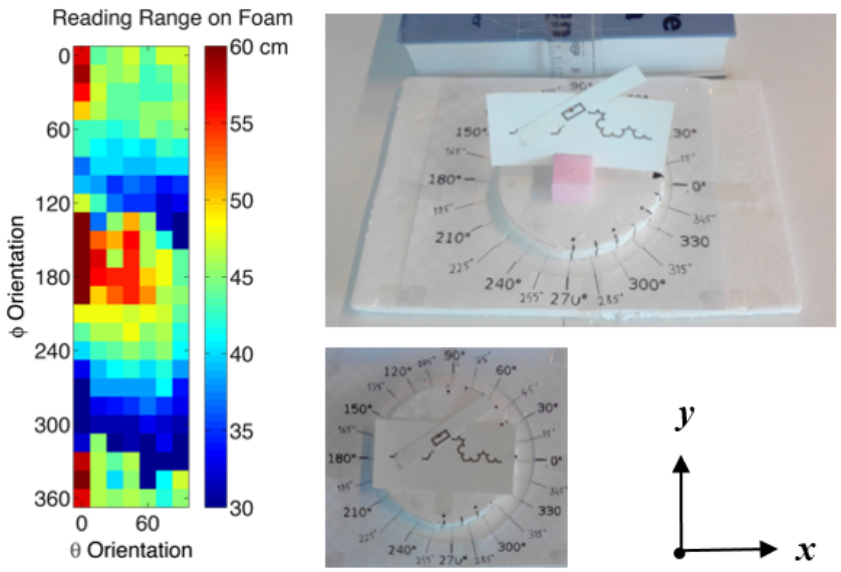



Figure 4.35: Reading tests on foam with fractal parasitic element

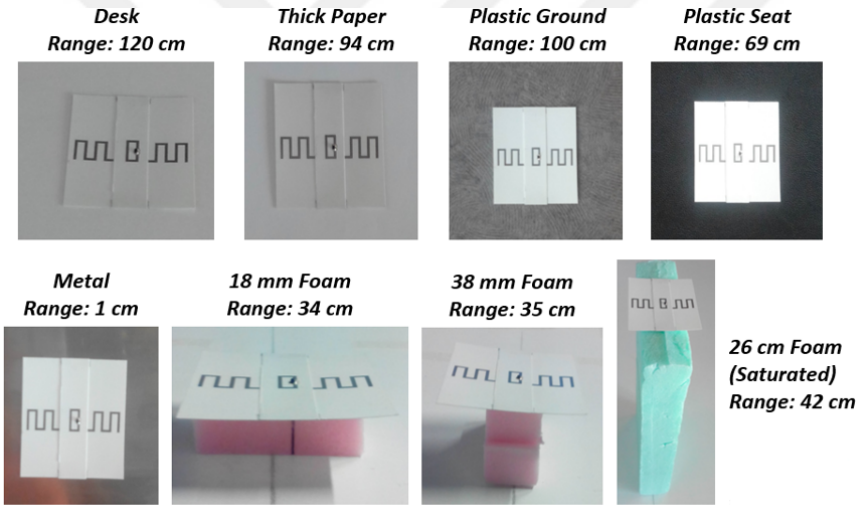



Figure 4.36: Reading ranges for the 6-turn loop-meander antenna when it is placed on different materials

antenna geometry is 3.2 cm × 7.9 cm as shown in Figure 4.43 with gap locations where blue triangles indicate the opened gaps. Power reflection coefficient and input impedance results for computational gaps are also shown in Figure 4.43.

Optimized values of the power reflection coefficient for calculated and modeled gaps are depicted in Figure 4.44. These two graphs are coherent with each other, while the modeled-gap results are closer to the real-life experiment.

| Rotation | 0° | 15° | 30° | 45° | 60° | 75° | 90° | 105° | 120° | 135° | 150° | 165° |
|---|---|---|---|---|---|---|---|---|---|---|---|---|
| Range-A (cm) | 27 | 47 | 52 | 49 | 54 | 71 | 73 | 71 | 77 | 51 | 50 | 33 |
| Range-B (cm) | 32 | 47 | 53 | 56 | 60 | 71 | 80 | 75 | 85 | 75 | 52 | 56 |
| Range-F (cm) | 0 | 12 | 30 | 35 | 51 | 54 | 69 | 63 | 73 | 47 | 25 | 44 |




Figure 4.37: Reading range of antennas on human body at two different positions

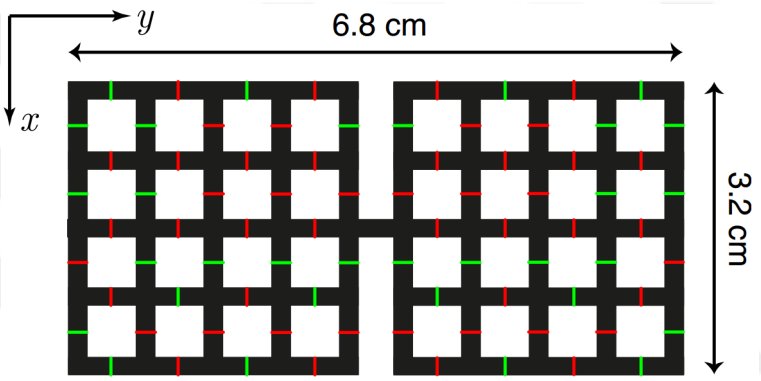



Figure 4.38: Geometry of cage-dipole antennas and gap locations. An optimized configuration is shown. Green and red colors represent short circuit (no gap) and open circuit (gap), respectively.

Antenna input impedance must be highly inductive to be matched conjugately to highly capacitive chip impedance. For a better matching, the reactive part of the input impedance of the antenna is adjusted by increasing the width of the antenna from 32 mm to 47 mm. Simulation results of the power reflection coefficient using the computational and modeled gaps are shown in Figure 4.45 and Figure 4.46. As can be seen in these figures, power reflection falls to -48.32 dB at 865 MHz using the computational gaps and -28.29 dB at 870 MHz using the modeled gaps, respectively. Conjugate matching with the chip impedance is obtained successfully at 865 MHz.

Finally a microchip is attached to a printed antenna terminals and reading ranges

Table4.1: Optimization Results for the Cage-Dipole Antennas Matching to 50 Ω

| Computational Gaps | | | Modeled Gaps | | |
|---|---|---|---|---|---|
| Cost Func. | $S_{11}$ (dB) | Directive Gain | Cost Func. | $S_{11}$ (dB) | Directive Gain |
| 1.9058 | -39.66 | 1.9258 | 1.6336 | -16.02 | 1.9824 |
| 1.7066 | -24.32 | 1.8172 | 1.6614 | -21.76 | 1.8092 |
| 1.9633 | -35.68 | 1.9961 | 1.6228 | -14.61 | 1.9935 |

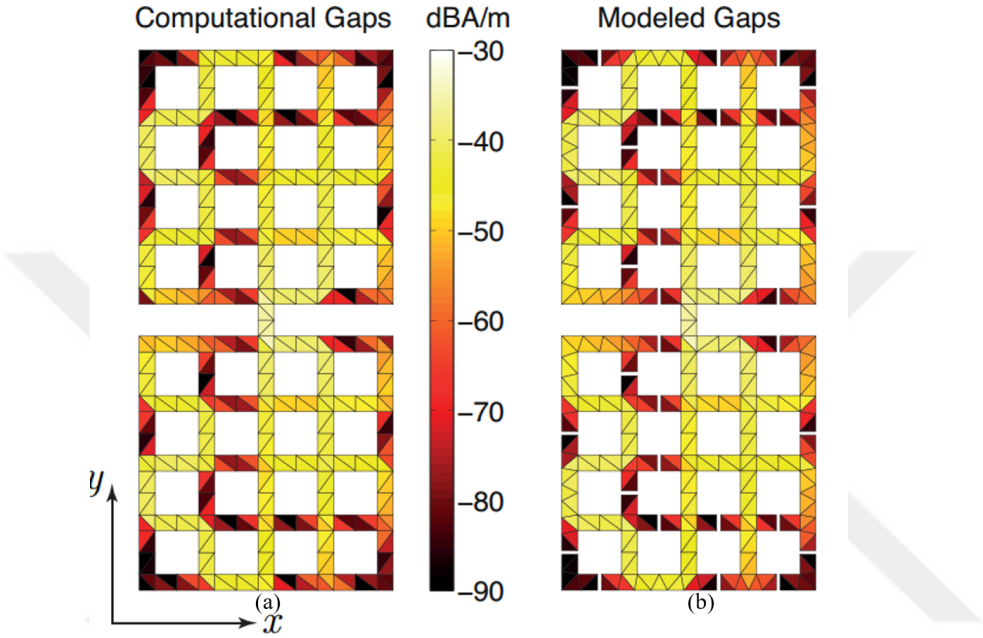



Figure 4.39: Current distributions on the cage-dipole antenna excited by 1V delta-gap source (a) computational gaps (b) modeled gaps

are measured by ATiD 870 Hand-Held UHF RFID reader. The measurement setup and reading range distribution as a colored graph are shown in Figure 4.47, along with the printed antenna. The measurements are conducted for $\theta$ from 0° to 180° and for $\phi$ from 0° to 360° with 15° steps. For each $\theta$ value, $x-y$ plane is scanned with 15° intervals to extract the reading-range pattern.

Reading range on human body tests with isolated tag are also measured and the results are depicted in Figure 4.48.

As it can be observed from the figures, antenna has considerably high reading range, reaching to 1.5 m in a wide band of observation angles. The read range value reaches 2.3 m at the maximum directions on human body tests; hence, the

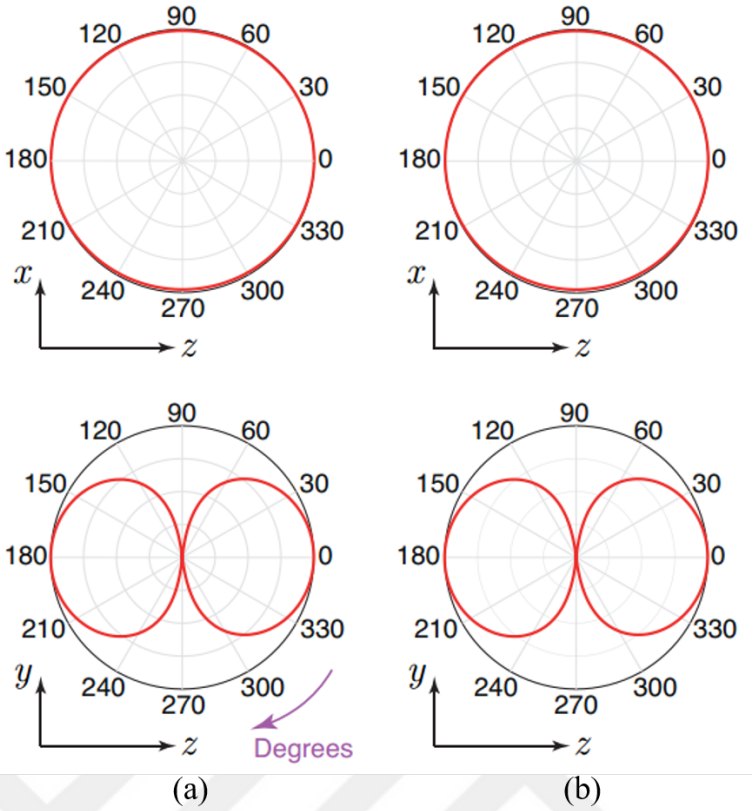



Figure 4.40: Radiation patterns of the cage-dipole antenna excited by 1V delta-gap source; using (a) computational gaps (b) modeled gaps

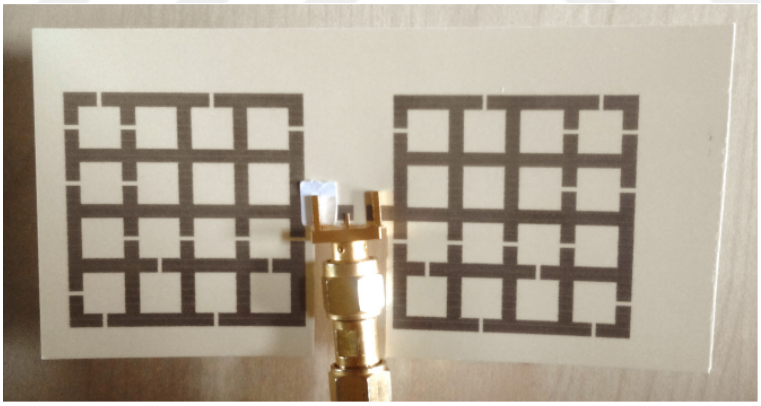


Figure 4.41: Measurement setup of the optimized cage-dipole antenna that is attached to a coaxial end with physical press

antenna is convenient for RFID applications, such as an access control application, since it can also fit on an ID card.

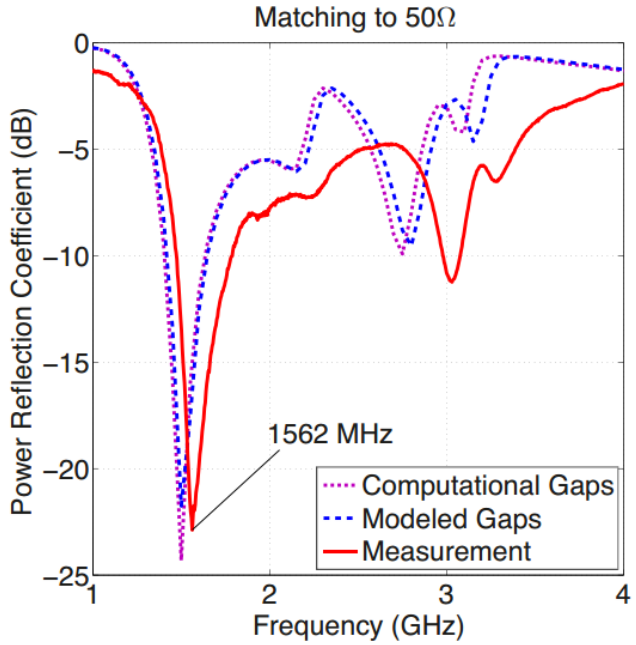



Figure 4.42: Simulation and measurement results for the optimized cage-dipole antenna from 1 GHz to 4 GHz

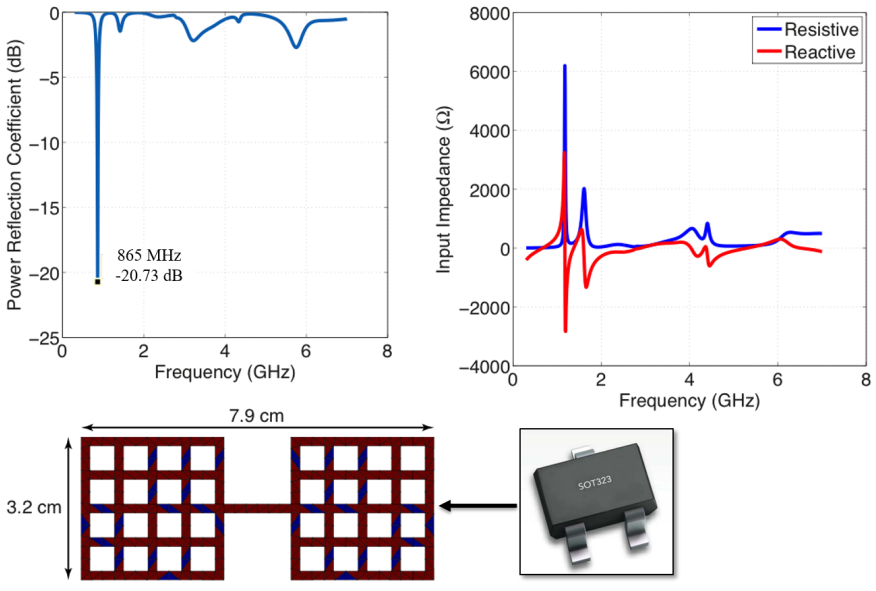



Figure 4.43: Simulation results of power reflection coefficient and input impedance of the RFID cage-dipole antenna from 0.3 GHz to 7 GHz

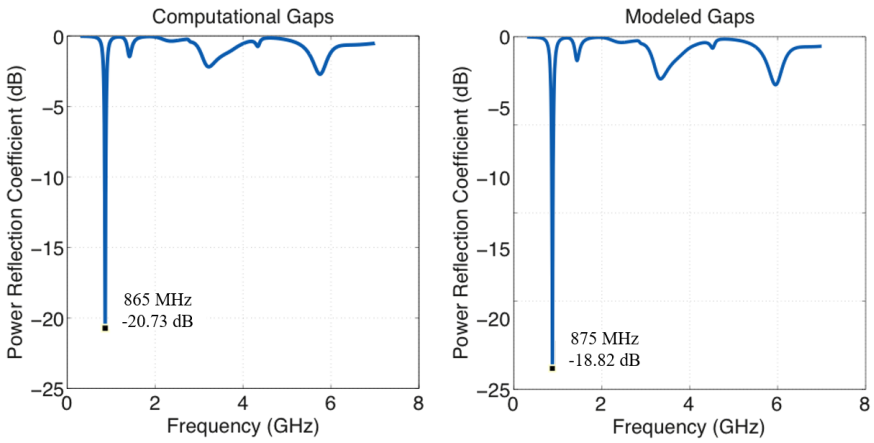



Figure 4.44: Power reflection coefficient results for the RFID cage-dipole antenna from 0.3 GHz to 7 GHz using calculated and modeled gaps

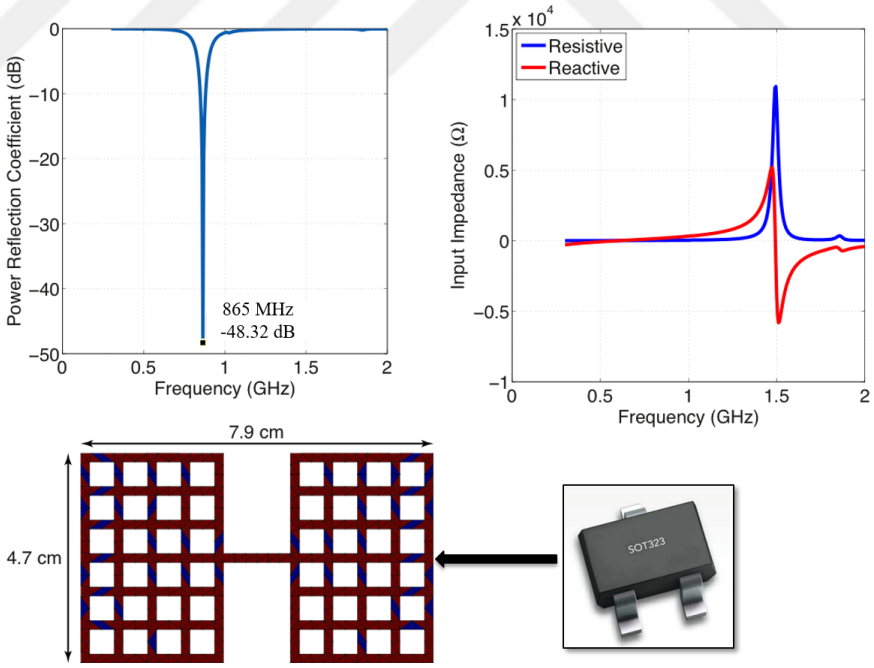



Figure 4.45: Power reflection coefficient and input impedance of the RFID cage-dipole antenna from 0.3 GHz to 2 GHz using computational and modeled gaps

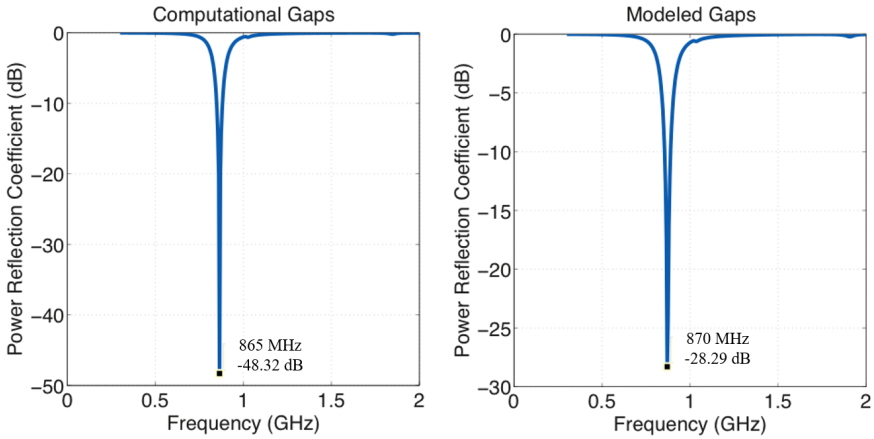



Figure 4.46: Power reflection coefficients for the 4.7 cm (width) RFID cage-dipole antenna from 0.3 GHz to 2 GHz using computational and modeled gaps

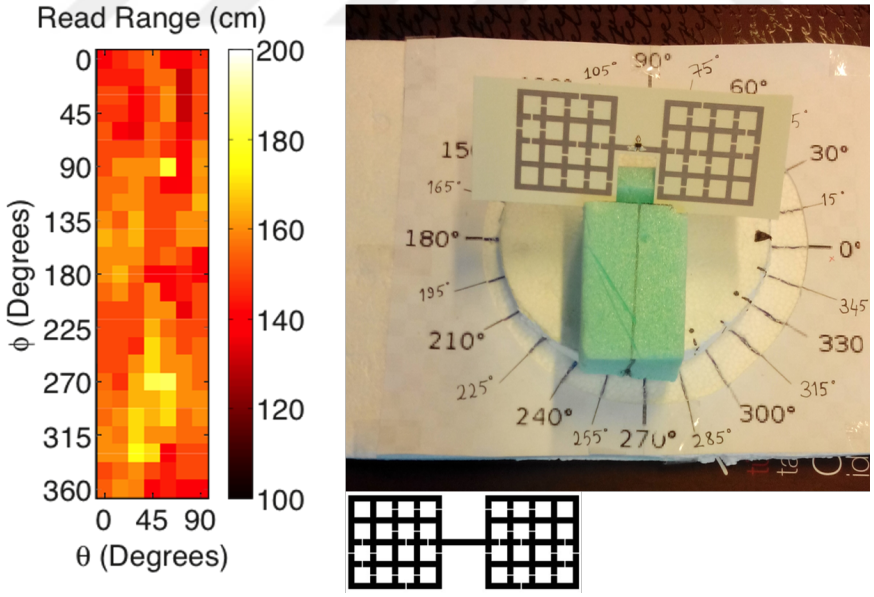



Figure 4.47: Reading range values for the optimized cage-dipole antenna obtained via measurements

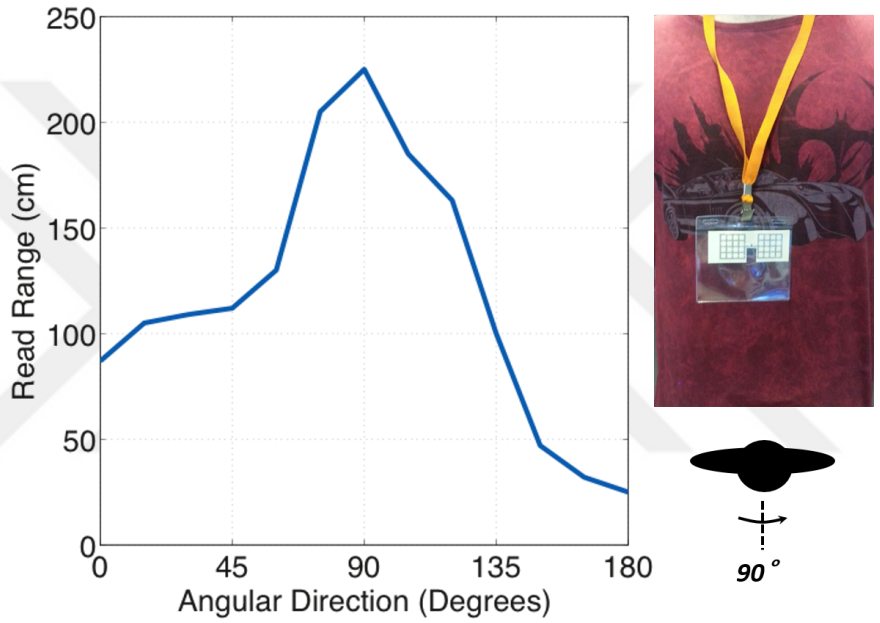



Figure 4.48: Reading range of the optimized RFID cage-dipole antenna on human body

# CHAPTER 5

# CONCLUSION AND FUTURE WORK

In this thesis, low-cost, compact, small size, and flexible inkjet antennas that are produced by using silver-based ink in standard printers are presented. Canon GP-501 normal photograph paper is used as the substrate. For a given geometry, dielectric characteristics of the paper are obtained by using an iterative procedure. As a consequence of experiments, the paper permittivity is found to be about $3.5 \times (1 + i0.06)$, while the effective permittivity (in MOM/MLFMA) depends on the antenna. Simulations are realized via MOM/MLFMA which present precise solutions. Steps of the inkjet printing routine are demonstrated in detail. Curing duration and effect of temperature in inkjet printing are investigated. The ideal temperature and curing time are found to be around 160° for 90 minutes. Four antenna types are investigated for RFID applications. The cost of each RFID tag, including the designed antenna and the IC microchip, is less than 1 USD.

As the first type, an S-monopole antenna with a size of 74 mm (width) x 94 mm (length) x 0.254 mm is fabricated on photograph paper. Designed antenna is tuned to operate at around 1.6 GHz with matching to 50 Ω. The same antenna is designed for RFID applications and conjugately matched to the microchip impedance. Simulation and measurement results are consistent with each other. On the other hand, the performance of the antenna is found to be unsatisfactory for RFID applications.

As the second type, a small size symmetrical circular dipole antenna is used and matched to 50 Ω input impedance. Measurement results show that the antenna

has good reflection coefficient values at 870 MHz, but only when matching to 50 Ω.

In order to design suitable RFID tags, we continue with a third type, namely, loop-meander antennas. First, loop antenna is designed with good match to the microchip impedance. Then, meander parasitic elements are added to the loop antenna to increase the reading range. Measurements verify successful reads that have 60 cm reading ranges.

As the fourth type, cage-dipole antennas are designed and optimized for both 50 Ω and chip impedances. Switches located on the structures are opened or closed according to the optimization results for desired characteristics. Measurement and simulation results for 50 Ω antenna are in good agreement with each other, providing good reflection coefficient values at around 1.5 GHz. In addition, the antenna that is matched to the chip impedance at 865 MHz provides very good read-range performance. Specifically, we obtain nearly omnidirectional reading pattern with 130 cm range at all directions. Reading range tests are also conducted on human body. It reaches to 230 cm in the maximum direction. The results demonstrate favorable properties of the cage-dipole antennas for RFID applications.

For future work, items below can be performed further:

• Different types of antennas can be designed and fabricated for RFID applications. Reading range of inkjet RFID antennas can be increased.

• Impedance measurement setup for RFID antennas can be developed with convenient UHF balun element especially for the dipole-type antennas.

• Inkjet antennas can be realized on various types of flexible substrates. They can be appropriate for textile antennas.

• Inkjet printing technology can be used for producing different microwave structures, like metamaterials.

# REFERENCES


[1] L. Yang, A. Rida, R. Vyas, and M. M. Tentzeris, "Rfid tag and rf structures on a paper substrate using inkjet-printing technology," *IEEE Transactions on Microwave Theory and Techniques*, vol. 55, pp. 2894–2901, Dec. 2007.

[2] Z. Konstas, A. Rida, R. Vyas, K. Katsibas, N. Uzunoğlu, and M. M. Tentzeris, "A novel inkjet-printed z-shaped monopole antenna for rfid applications," in *3rd European Conference on Antennas and Propagation*, pp. 2340–2343, Mar. 2009.

[3] A. Rida, L. Yang, R. Vyas, and M. M. Tentzeris, "Conductive inkjet-printed antennas on flexible low-cost paper-based substrates for rfid and wsn applications," *IEEE Antennas and Propagation Magazine*, vol. 51, pp. 13–23, June 2009.

[4] M. Marroncelli, D. Trinchero, and M. M. Tentzeris, "Paper-based, inkjet-printed, text-meandered uhf resonant antennas for rfid applications," in *General Assembly and Scientific Symposium, 2011 th URSI*, pp. 1–4, Aug. 2011.

[5] B. S. Cook and A. Shamim, "Inkjet printing of novel wideband and high gain antennas on low-cost paper substrate," *IEEE Transactions on Antennas and Propagation*, vol. 60, pp. 4148–4156, Sep. 2012.

[6] A. R. Maza, B. Cook, G. Jabbour, and A. Shamim, "Paper-based inkjet-printed ultra-wideband fractal antennas," *IET Microwaves, Antennas Propagation*, vol. 6, pp. 1366–1373, Sep. 2012.

[7] H. F. Abutarboush and A. Shamim, "Paper-based inkjet-printed tri-band u-slot monopole antenna for wireless applications," *IEEE Antennas and Wireless Propagation Letters*, vol. 11, pp. 1234–1237, Oct. 2012.

[8] A. A. Babar, J. Virtanen, V. A. Bhagavati, L. Ukkonen, A. Z. Elsherbeni, P. Kallio, and L. Sydänheimo, "Inkjet-printable uhf rfid tag antenna on a flexible ceramic-polymer composite substrate," in *Microwave Symposium Digest (MTT), 2012 IEEE MTT-S International*, pp. 1–3, June 2012.

[9] G. Tarapata, D. Paczesny, and K. Kawecki, "Characterization of inkjet-printing hf and uhf antennas for rfid applications," in *Proc. SPIE*, vol. 8903, pp. 32–38, 2013.

[10] H. F. Abutarboush, M. F. Farooqui, and A. Shamim, "Inkjet-printed wideband antenna on resin-coated paper substrate for curved wireless devices," *IEEE Antennas and Wireless Propagation Letters*, vol. 15, pp. 20–23, 2016.

[11] C. Onol, T. Ciftçi, S. Küçük, B. Karaosmanoglu, and Ö. Ergül, "Design, simulation, and fabrication of low-cost inkjet antennas," in *Proc. Progress in Electromagnetics Research Symp. (PIERS)*, pp. 2829–2833, 2015.

[12] G. Shaker, S. Safavi-Naeini, N. Sangary, and M. M. Tentzeris, "Inkjet printing of uwb antennas on paper-based substrates," *IEEE Antennas and Wireless Propagation Letters*, vol. 10, pp. 111–114, 2011.

[13] C. A. Balanis, *Antenna Theory: Analysis and Design*. Wiley-Interscience, 2005.

[14] D. M. Dobkin, *The RF in RFID: Passive UHF RFID in Practice*. Newton, MA, USA: Newnes, 2007.

[15] J. Kimionis, M. M. Tentzeris, and S. Nikolaou, "Inkjet-printed uhf rfid folded dipole antennas for remote sensing applications," in *2014 IEEE Antennas and Propagation Society International Symposium (APSURSI)*, pp. 332–333, July 2014.

[16] B. Karaosmanoğlu, T. Çiftçi, and Ö. Ergül, "Challenges in low-cost inkjet antennas," in *Radio Science Meeting (Joint with AP-S Symposium), 2015 USNC-URSI*, p. 181, July 2015.

[17] Ö. Ergül and L. Gürel, *The Multilevel Fast Multipole Algorithm (MLFMA) for Solving Large-Scale Computational Electromagnetics Problems*. 1st ed., 2014.

[18] K. Finkenzeller, *RFID Handbook: Fundamentals and Applications in Contactless Smart Cards and Identification*. Wiley Publishing, 2nd ed., 2003.

[19] J.-P. Curty, M. Declercq, C. Dehollain, and N. Joehl, *Design and Optimization of Passive UHF RFID Systems*. Springer Publishing Company, Incorporated, 1st ed., 2010.

[20] K. V. S. Rao, P. V. Nikitin, and S. F. Lam, "Antenna design for uhf rfid tags: a review and a practical application," *IEEE Transactions on Antennas and Propagation*, vol. 53, pp. 3870–3876, Dec. 2005.

[21] C.-H. Loo, K. Elmahgoub, F. Yang, A. Z. Elsherbeni, D. Kajfez, A. A. Kishk, T. Elsherbeni, L. Ukkonen, L. Sydanheimo, M. Kivikoski, *et al.*, "Chip impedance matching for uhf rfid tag antenna design," *Progress In Electromagnetics Research*, vol. 81, pp. 359–370, 2008.

[22] V. D. Hunt, A. Puglia, and M. Puglia, *RFID: A Guide to Radio Frequency Identification*. Wiley-Interscience, John Wiley & Sons Inc., 2007.

[23] K. V. S. Rao, P. V. Nikitin, and S. F. Lam, "Impedance matching concepts in rfid transponder design," in *Fourth IEEE Workshop on Automatic Identification Advanced Technologies (AutoID'05)*, pp. 39–42, Oct. 2005.

[24] E. Tekin, P. J. Smith, and U. S. Schubert, "Inkjet printing as a deposition and patterning tool for polymers and inorganic particles," *Soft Matter*, vol. 4, pp. 703–713, 2008.

[25] M. Singh, H. M. Haverinen, P. Dhagat, and G. E. Jabbour, "Inkjet printing process and its applications," *Advanced materials*, vol. 22, no. 6, pp. 673–685, 2010.

[26] K. Kurokawa, "Power waves and the scattering matrix," *IEEE Transactions on Microwave Theory and Techniques*, vol. 13, pp. 194–202, Mar. 1965.

[27] P. V. Nikitin, K. V. S. Rao, S. F. Lam, V. Pillai, R. Martinez, and H. Heinrich, "Power reflection coefficient analysis for complex impedances in rfid tag design," *IEEE Transactions on Microwave Theory and Techniques*, vol. 53, pp. 2721–2725, Sep. 2005.